BPR MCS
Bulletin of Pioneering Researches of Medical and Clinical Science

Bulletin of Pioneering Researches of Medical and Clinical Science

Available online: https://bprmcs.com
2025 | Volume 5 | Issue 2 | Page: 202-223

Rational Development of NAMPT/PARP1 Dual Inhibitors Targeting NAD Metabolism for Breast Cancer Therapy

Jinwoo Park[1]*, Minji Kim[1], Seung Lee[2]

[1]Department of Medical and Translational Sciences, Seoul National University, Seoul, South Korea.
[2]Department of Clinical Innovation and Biomedical Analytics, KAIST, Daejeon, South Korea.

Abstract

The global burden of breast cancer remains formidable, as current therapeutic regimens frequently fail to achieve optimal outcomes. A growing body of evidence supports targeting nicotinamide adenine dinucleotide (NAD) metabolism—a molecule indispensable to the viability and expansion of malignant cells—as a compelling anticancer strategy. In mammalian systems, maintaining adequate NAD pools depends on two principal enzymes: nicotinamide phosphoribosyltransferase (NAMPT) and poly(ADP-ribose) polymerase 1 (PARP1). Recent investigations have drawn attention to the potential therapeutic gain from pairing NAMPT inhibitors with PARP1 inhibitors, particularly for breast cancer. In the present study, a series of eleven unprecedented NAMPT/PARP1 dual-target inhibitors was conceived and prepared. One analog, designated DDY02, displayed tolerable potency against both enzymatic targets, registering IC50 values of 0.01 and 0.05 μM, respectively. Moreover, in vitro profiling demonstrated that exposure to DDY02 triggered suppressed cell growth, NAD diminution, DNA lesions, programmed cell death, and reduced migratory capacity in MDA-MB-468 cells. Collectively, these data position DDY02—acting on NAD metabolism by concurrently blocking NAMPT and PARP1—as a promising lead structure for breast cancer treatments.

Keywords: NAMPT, PARP1, NAD, Dual-target inhibitors, Breast cancer

Corresponding author: Jinwoo Park
E-mail: jinwoo.park@outlook.com

Received: 02 June 2025
Revised: 27 August 2025
Accepted: 01 September 2025

How to Cite This Article: Park J, Kim M, Lee S. Rational Development of NAMPT/PARP1 Dual Inhibitors Targeting NAD Metabolism for Breast Cancer Therapy. Bull Pioneer Res Med Clin Sci. 2025;5(2):202-23. https://doi.org/10.51847/hc2kBDACqu

Introduction

Nicotinamide adenine dinucleotide (NAD) serves as an essential coenzyme for the shuttle of hydrogen atoms and electrons during redox transformations, exerting a fundamental influence not only on core metabolic circuits such as glycolysis, the tricarboxylic acid cycle, and oxidative phosphorylation, but also on serine biosynthesis [1]. This functional breadth helps satisfy the voracious energy and macromolecular precursor requirements characterizing cancer cells. Following malignant conversion, enzymes dependent on NAD—encompassing poly(ADP-ribose) polymerases (PARPs), mono(ADP-ribosyl)transferases (Marts), sirtuins (Sirt1-7), and cyclic ADP-ribose (cADPR) synthases (CD38 and CD157)—become hyperactivated [2]. Such upregulation supports neoplastic cells in maintaining genomic integrity, driving oncogene transcription, and evading immune surveillance, all at the cost of escalated NAD turnover [3]. Cancer cells consequently exhibit a heightened dependence on NAD, rendering them uniquely sensitive to perturbations in NAD homeostasis—a vulnerability that has been therapeutically validated.

De novo construction of NAD from L-tryptophan proceeds via a multistep enzymatic cascade. Yet this route

alone seldom accommodates the urgent cellular requisition for NAD. Nicotinic acid (NA) and nicotinamide (NAM), alternative vitamers of vitamin B3, serve as critical building blocks for NAD biosynthesis. Although mammals have preserved the Preiss–Handler axis employing NA, they predominantly resort to the salvage route centered on NAM, owing to its superior efficiency and rapidity [4].

Nicotinamide phosphoribosyltransferase (NAMPT) serves as the pace-setting catalyst within the salvage pathway, orchestrating the condensation of NAM with PRPP to yield nicotinamide mononucleotide (NMN) [5]. Ever since FK866 (compound 1) **(Figure 1)** emerged in 2002 as a high-affinity NAMPT inhibitor active at nanomolar concentrations, diverse NAMPT inhibitors have emerged from both academic laboratories and industrial pipelines [6-8]. Nonetheless, pioneering candidates such as FK866 and CHS828 (compound 2) **(Figure 1)** were abandoned during phase II evaluation, victims of suboptimal potency, intolerable dose-dependent toxicities, and unsatisfactory pharmacokinetics. More recently, OT-82 (compound 3) **(Figure 1)**, built around a distinct chemotype, was disclosed in 2019 and is presently being assessed in phase I trials for hematologic malignancies [9].

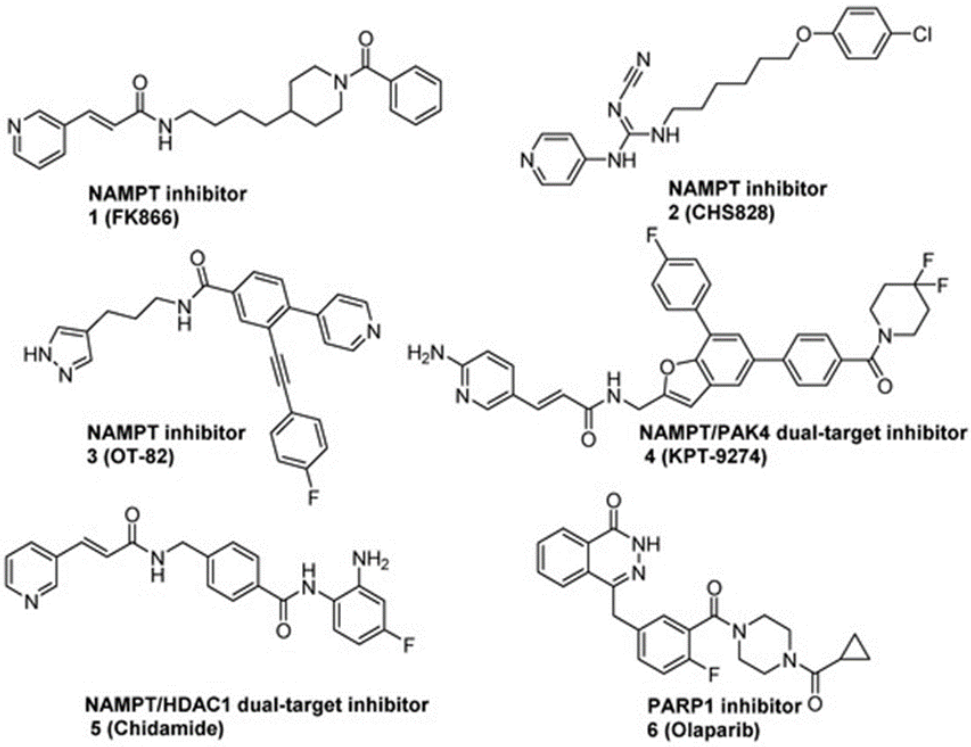

Figure 1. The structures of NAMPT inhibitors and PARP1 inhibitors.

Tumors exhibit profound molecular heterogeneity, and single-pathway interdiction often translates into restrained clinical benefit. Dual-target agents, which engage two distinct nodes simultaneously, hold the capacity to elicit cooperative antitumor effects and are gaining traction as next-generation oncological interventions [10]. Contemporary scholarship has spotlighted the promise of bispecific NAMPT ligands for upgrading therapeutic responses [6]. For example, KPT-9274 (compound 4) **(Figure 1)**, a hybrid inhibitor of NAMPT and p21-associated kinase 4 (PAK4), has advanced into human trials for malignancy. Strikingly, Chidamide (compound 5) **(Figure 1)**, originally approved by the CFDA in 2014 as a histone deacetylase antagonist for lymphoma, was retrospectively recognized as a dual NAMPT/HDAC inhibitor [11]. Dual-pharmacophore NAMPT ligands may therefore command an edge over their monospecific counterparts in oncological applications.

PARP1 harnesses NAD as a co-substrate to direct the poly(ADP-ribosyl)ation of acceptor proteins, a cornerstone mechanism for rectifying single-strand breaks in DNA [12]. The exceptional proliferative rate of cancer cells imposes a greatly intensified DNA damage stress relative to normal tissues, engendering an acute dependence on DNA repair machinery. PARP1 inhibitors exploit the synthetic lethality paradigm to eradicate tumor cells harboring defects in homologous recombination selectively [13, 14]. Beginning with the registration of Olaparib (compound 6) **(Figure 1)** in 2014 as the first-in-class PARP1 inhibitor for ovarian carcinoma, a total of six PARP1 inhibitors have entered the market. Clinical experience, however, has highlighted shortcomings, including limited effectiveness, significant adverse-event profiles, and the emergence of refractory disease. To circumvent these challenges, medicinal chemists have pioneered an array of dual-target PARP1 inhibitors. These

bifunctional molecules are postulated to achieve pharmacodynamic synergy with PARP1 blockade by impairing homologous recombination or inducing additional DNA damage [15].

Notably, the tight functional coupling among NAMPT, PARP1, and NAD metabolism provides a compelling rationale for engineering dual-target inhibitors that simultaneously target both nodes. PARP1 activity drains cellular NAD reserves, directly yoking DNA repair machinery to NAD homeostasis. Thus, NAMPT and PARP1 are intertwined in their roles in preserving NAD availability and in mounting an appropriate response to genotoxic insults. Perturbation of either enzyme's activity can alter NAD levels, with downstream consequences for cell survival, bioenergetics, and the capacity to withstand DNA-damage stress. This reciprocal reliance cements their status as attractive therapeutic targets in oncology. PARP1 inhibitors used in the clinic typically act by competing with the substrate NAD. Lowering NAD abundance via NAMPT inhibition amplifies the blocking potency of PARP1 inhibitors, constituting a novel mode of synergy [16]. Indeed, pairing NAMPT inhibitors with PARP1 inhibitors has yielded synergistic antitumor effects across diverse cancer types, including breast cancer, Ewing sarcoma, and ovarian cancer [17-19]. This promising avenue has the potential to address the limitations of conventional PARP1 inhibitors and enhance overall treatment efficacy.

In 2019, a patent described a series of phthalazinone-containing compounds as PARP1 inhibitors (compounds 7 and 8) **(Figure 2)** that displayed remarkable growth-suppressive activity against Olaparib-refractory MDA-MB-468 cells [20]. While the patent did not explicitly identify NAMPT as a target, pharmacophore screening suggests that these molecules may act as dual-target inhibitors of NAMPT and PARP1. We reason that their pronounced ability to circumvent drug resistance arises from co-inhibition of NAMPT and PARP1. Later, in 2021, a separate patent disclosed compounds built around the identical core scaffold as highly potent NAMPT/PARP1 dual-target inhibitors (compounds 9 and 10) **(Figure 2)**, exhibiting strong anti-proliferative activity against a panel of three breast cancer cell lines [21].

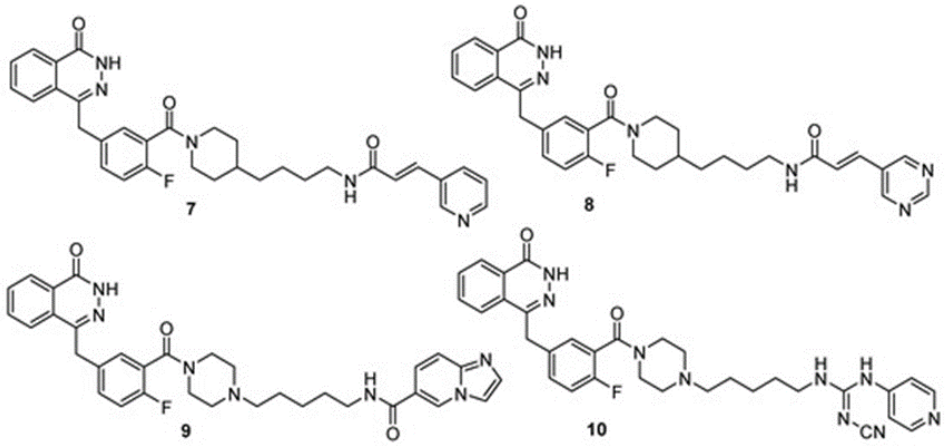

Figure 2. The structures of NAMPT/PARP1 dual-target inhibitors from patents.

To this point, the peer-reviewed literature has remained silent on the deliberate design of NAMPT/PARP1 dual-target inhibitors, and the patent record alone offers scant insight into the therapeutic advantages conferred by this emerging inhibitor class in oncology. Against this backdrop, our investigation aimed to design and prepare 11 NAMPT/PARP1 dual-target inhibitors featuring unprecedented core architectures. We have systematically charted the structure–activity relationships and rigorously examined their efficacy and mode of action within breast cancer models. We trust that this body of work will stand as a useful reference, deepening the conceptual framework and the practical deployment of NAD metabolism-targeting in cancer therapy.

Materials and Methods

Chemistry

The convergent synthetic route to the target compounds is outlined in Scheme 1. Commercially sourced 1-Boc-piperazine 18 underwent sulfonylation with sulfonyl chlorides 19–20 to deliver intermediates 21–22. The pendant nitroarenes 21–22 were then reduced under a hydrogen atmosphere over palladium on carbon, yielding anilines 23–24. Exposure of 23 to thiophosgene, with subsequent nucleophilic addition of pyridin-3-ylmethanamine, installed the thiourea linkage of intermediate 25. For the corresponding urea derivatives 26–27, intermediates 23–24 were activated with triphosgene and then trapped with pyridin-3-ylmethanamine under an analogous reaction manifold. Acidolytic removal of the Boc groups with trifluoroacetic acid liberated the amine intermediates 28–30. Concurrently, the carboxylic acid building blocks P1–P4

were prepared according to published protocols [22-25]. Amide bond construction between these acid fragments and intermediates 28–30, mediated by EDCI/HOBT/TEA in DMF, completed the assembly of the final compound series DDY01–DDY11.

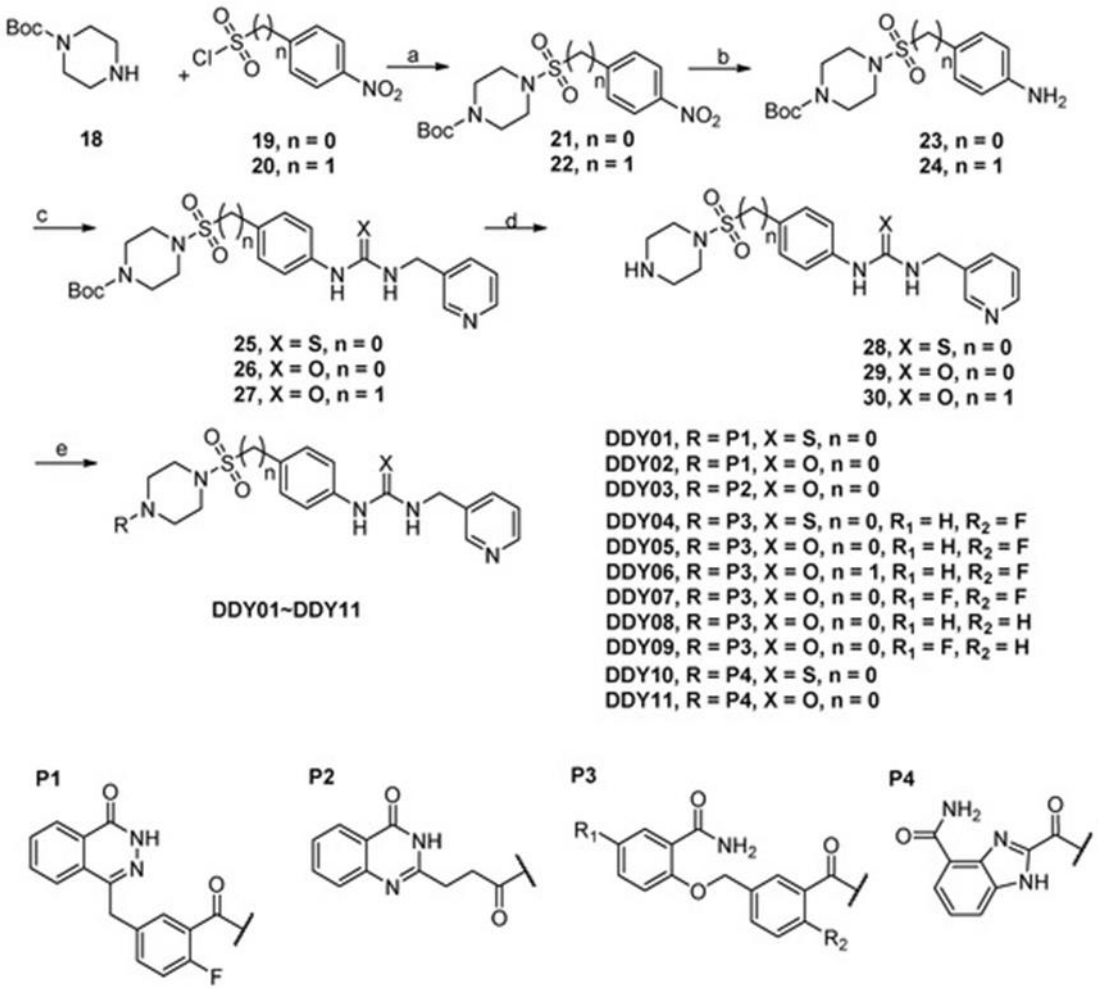

Scheme 1. Synthesis of designed NAMPT/PAPR1 dual-target inhibitors. Reagents and conditions: (a) pyridine/DCM (1:1), rt, 2 h; (b) Pd/C, H2, EtOAc, rt, 12 h; (c) thiophosgene or triphosgene, NaHCO3, CH2Cl2, C2H5OH, rt, 1 h; (d) TFA, CH2Cl2, rt,1 h; (e) EDCI, HOBT, TEA, DMF, rt, overnight.

tert-butyl 4-((4-nitrophenyl)sulfonyl)piperazine-1-carboxylate (compound 21)

A solution of 18 (170 mg, 0.9 mmol) in tetrahydrofuran (5 mL) and pyridine (3 mL) was charged with 4-nitrobenzenesulfonyl chloride (200 mg, 0.9 mmol) at 25 °C, and the mixture was warmed to 60 °C with continued stirring for 30 min. The reaction was diluted with dichloromethane (20 mL), and the organic phase was washed with 2 N HCl (10 mL), then with brine (20 mL), and dried over anhydrous Na2SO4. Filtration, removal of volatiles under reduced pressure, and purification by silica gel column chromatography (petroleum ether/ethyl acetate = 1/2) yielded intermediate 21 (279 mg, 83%) as a white solid. Melting point: 106–107 °C; 1H NMR (400 MHz, DMSO-d6) δ 8.44 (d, J = 8.8 Hz, 2H), 8.01 (d, J = 8.8 Hz, 2H), 3.41 (t, J = 5.1 Hz, 4H), 2.96 (t, J = 5.0 Hz, 4H), 1.34 (s, 9H). HRMS (ESI) m/z calculated for C15H21N3O6S [M + H]+ 372.1229, found 372.1223.

tert-butyl 4-((4-nitrobenzyl)sulfonyl)piperazine-1-carboxylate (compound 22)

Replacement of 4-nitrobenzenesulfonyl chloride with (4-nitrophenyl)methanesulfonyl chloride, with all other conditions matching those outlined for 21, afforded compound 22 as a white solid; yield: 18%; melting point: 133–134 °C; 1H NMR (400 MHz, DMSO-d6) δ 8.26 (d, J = 8.7 Hz, 2H), 7.69 (d, J = 8.8 Hz, 2H), 4.65 (s, 2H), 3.36 (t, J = 5.1 Hz, 4H), 3.13 (t, J = 5.0 Hz, 4H), 1.41 (s, 9H). HRMS (ESI) m/z calculated for C16H23N3O6S [M − H]− 384.1234, found 384.1238.

tert-butyl 4-((4-aminophenyl)sulfonyl)piperazine-1-carboxylate (compound 23)

Intermediate 21 (2.8 g, 0.7 mmol) was dissolved in methanol (10 mL), and palladium on carbon (0.28 g, 10% w/w) was introduced. The suspension was stirred under a

hydrogen atmosphere (1 atm) at 25 °C for 8 h. The catalyst was filtered off, the filtrate was concentrated in vacuo, and the residual material was purified by silica gel column chromatography (dichloromethane/methanol = 40/1) to give intermediate 23 (2.36 g, 92%) as a white solid. Melting point: 180–181 °C; 1H NMR (400 MHz, DMSO-d6) δ 8.91 (d, J = 141.3 Hz, 2H), 7.49 (d, J = 8.1 Hz, 2H), 6.93 (s, 2H), 3.38 (s, 4H), 2.77 (s, 4H), 1.35 (s, 9H). HRMS (ESI) m/z calculated for C15H23N3O4S [M + Na]+ 364.1307, found 364.1300.

tert-butyl 4-((4-aminobenzyl)sulfonyl)piperazine-1-carboxylate (compound 24)

Using compound 22 as substrate and applying the hydrogenation protocol described for the synthesis of 23 furnished compound 24 as a white solid; yield: 53%; melting point: 133–134 °C; 1H NMR (400 MHz, DMSO-d6) δ 7.02 (d, J = 8.4 Hz, 2H), 6.53 (d, J = 8.4 Hz, 2H), 5.19 (s, 2H), 4.18 (s, 2H), 3.30 (t, J = 5.1 Hz, 4H), 3.11–2.87 (m, 4H), 1.40 (s, 9H). HRMS (ESI) m/z calculated for C16H25N3O4S [M + Na]+ 378.1463, found 378.1459.

tert-butyl 4-((4-(3-(pyridin-3-ylmethyl)thioureido)phenyl)sulfonyl)piperazine-1-carboxylate (compound 25)

An aqueous solution (5 mL) of NaHCO3 (0.15 g, 1.8 mmol) was charged with 23 (0.34 g, 0.9 mmol) and thiophosgene (0.13 g, 1.1 mmol), and the mixture was agitated at 25 °C for 10 min. Dichloromethane (5 mL) was subsequently introduced, and stirring was maintained at 25 °C for a further 2 h. The reaction was then diluted with additional dichloromethane (15 mL), after which the organic phase was washed sequentially with water (30 mL) and brine (30 mL) and dried over anhydrous Na2SO4. Filtration and solvent removal under reduced pressure were followed by silica gel column chromatography (dichloromethane/methanol = 40/1) to yield intermediate 25 (0.33 g, 76%) as a white solid. Melting point: 127–128 °C; 1H NMR (400 MHz, DMSO-d6) δ 10.13 (s, 1H), 8.62 (t, J = 5.8 Hz, 1H), 8.58 (d, J = 2.2 Hz, 1H), 8.48 (d, J = 3.1 Hz, 1H), 7.81 (d, J = 8.8 Hz, 2H), 7.77 (d, J = 7.9 Hz, 1H), 7.66 (d, J = 8.9 Hz, 2H), 7.42–7.33 (m, 1H), 4.79 (d, J = 5.6 Hz, 2H), 3.40 (t, J = 5.0 Hz, 4H), 2.84 (t, J = 5.0 Hz, 4H), 1.34 (s, 9H). HRMS (ESI) m/z calculated for C22H29N5O4S2 [M + H]+ 492.1734, found 492.1738.

tert-butyl 4-((4-(3-(pyridin-3-ylmethyl)ureido)phenyl)sulfonyl)piperazine-1-carboxylate (compound 26)

Prepared from intermediate 23 following a route analogous to that set forth for 25, compound 26 was isolated as a white solid; yield: 33%; melting point: 151–152 °C; 1H NMR (400 MHz, DMSO-d6) δ 9.21 (s, 1H), 8.54 (d, J = 2.2 Hz, 1H), 8.46 (d, J = 4.8 Hz, 1H), 7.72 (d, J = 7.8 Hz, 1H), 7.66 (d, J = 6.8 Hz, 1H), 7.58 (d, J = 8.9 Hz, 2H), 7.40–7.32 (m, 1H), 6.92 (t, J = 6.0 Hz, 1H), 4.35 (d, J = 5.9 Hz, 2H), 3.38 (t, J = 5.0 Hz, 4H), 2.80 (t, J = 5.0 Hz, 4H), 1.34 (s, 9H). HRMS (ESI) m/z calculated for C22H29N5O5S [M + H]+ 476.1962, found 476.1975.

tert-butyl 4-((4-(3-(pyridin-3-ylmethyl)ureido)benzyl)sulfonyl)piperazine-1-carboxylate (Compound 27)

The synthesis of 27 was carried out starting from intermediate 24 under conditions essentially identical to those described for 25. The product was obtained as a yellow solid; yield: 50%; melting point: 141–142 °C; 1H NMR (400 MHz, DMSO-d6) δ 8.72 (s, 1H), 8.50 (d, J = 27.2 Hz, 2H), 7.72 (d, J = 9.8 Hz, 1H), 7.41 (d, J = 8.5 Hz, 2H), 7.39–7.34 (m, 1H), 7.25 (d, J = 8.3 Hz, 2H), 6.74 (t, J = 6.0 Hz, 1H), 4.32 (d, J = 5.8 Hz, 4H), 3.43–3.25 (m, 4H), 3.05 (t, J = 5.0 Hz, 4H), 1.40 (s, 9H). HRMS (ESI) m/z calculated for C23H31N5O5S [M + H]+ 490.2119, found 490.2126.

1-(4-(piperazin-1-ylsulfonyl)phenyl)-3-(pyridin-3-ylmethyl)thiourea (compound 28)

Trifluoroacetic acid (1.50 g, 13.4 mmol) was added dropwise to a stirred solution of 25 (0.33 g, 0.67 mmol) in dichloromethane (10 mL), and the reaction was stirred under a nitrogen blanket at 25 °C for 4 h. The mixture was subsequently washed with saturated aqueous NaHCO3 (60 mL) and brine (30 mL), then dried over anhydrous Na2SO4. Filtration and concentration under reduced pressure afforded intermediate 28 (0.17 g, 65%) as a white solid requiring no further purification. Melting point: 84–85 °C; 1H NMR (400 MHz, DMSO-d6) δ 8.96 (t, J = 5.8 Hz, 1H), 8.72 (s, 1H), 8.57 (d, J = 2.2 Hz, 1H), 8.48 (d, J = 6.4 Hz, 1H), 7.91 (d, J = 8.5 Hz, 2H), 7.76 (d, J = 7.9 Hz, 1H), 7.70 (d, J = 8.6 Hz, 2H), 7.46–7.29 (m, 1H),4.80 (d, J = 5.6 Hz, 2H), 3.34 (s, 1H), 3.20 (t, J = 5.0 Hz, 4H), 3.10 (d, J = 2.7 Hz, 4H). HRMS (ESI) m/z calculated for C17H21N5O2S2 [M + H]+ 392.1209, found 392.1203.

1-(4-(piperazin-1-ylsulfonyl)phenyl)-3-(pyridin-3-ylmethyl)urea (compound 29)

Compound 26 was subjected to the same Boc-deprotection protocol as outlined for 28, delivering compound 29 as a white solid; yield: 74%; melting point: 102–103 °C; 1H NMR (400 MHz, DMSO-d6) δ 9.23 (d, J = 2.5 Hz, 1H), 8.53 (d, J = 2.2 Hz, 1H), 8.46 (d, J = 6.4 Hz, 1H), 7.71 (d, J = 7.8 Hz, 1H), 7.65 (d, J = 8.9 Hz, 2H), 7.57 (d, J = 8.9 Hz, 2H), 7.39–7.35 (m, 1H), 6.96 (t, J = 4.3 Hz, 1H), 4.34 (d, J = 5.8 Hz, 2H), 3.16 (s, 1H), 2.73 (d, J = 7.7 Hz, 4H), 2.70 (d, J = 4.8 Hz, 4H). HRMS (ESI) m/z calculated for C17H21N5O3S [M + H]+ 376.1438, found 376.1434.

1-(4-((piperazin-1-ylsulfonyl)methyl)phenyl)-3-(pyridin-3-ylmethyl)urea (compound 30)

Intermediate 27 was processed under deprotection conditions matching those used for 28, providing compound 30 as a white solid; yield: 85%; melting point: 158–159 °C; 1H NMR (400 MHz, DMSO-d6) δ 9.51 (s, 1H), 9.41 (s, 2H), 8.84 (d, J = 2.0 Hz, 1H), 8.81 (d, J = 4.3 Hz, 2H), 8.52–8.45 (m, 1H), 8.06–7.98 (m, 1H), 7.44 (d, J = 8.6 Hz, 2H), 7.38 (t, J = 6.0 Hz, 1H), 7.28 (d, J = 8.6 Hz, 2H), 4.50 (d, J = 5.3 Hz, 2H), 4.43 (s, 2H), 3.32 (d, J = 2.7 Hz, 4H), 3.04 (s, 4H). HRMS (ESI) m/z calculated for C18H23N5O3S [M + H]+ 390.1594, found 390.1589.

1-(4-((4-(2-fluoro-5-((4-oxo-3,4-dihydrophthalazin-1-yl)methyl)benzoyl)piperazin-1-yl)sulfonyl)phenyl)-3-(pyridin-3-ylmethyl)thiourea (compound DDY01)

2-Fluoro-5-((4-oxo-3,4-dihydrophthalazin-1-yl)methyl)benzoic acid (0.24 g, 0.8 mmol) was dissolved in N,N-dimethylformamide (5 mL), and to this solution were added EDCI (0.16 g, 0.8 mmol), HOBt (0.12 g, 0.8 mmol), and DIPEA (0.23 mL, 1.38 mmol). The resulting mixture was stirred at 25 °C for 2 h, at which point 28 (0.31 g, 0.8 mmol) was introduced. Agitation was continued at 25 °C for 12 h, after which the reaction mixture was poured into dichloromethane (20 mL). The organic layer was washed with water (30 mL), then with brine (30 mL), and dried over anhydrous Na2SO4. After filtration and concentration under reduced pressure, the crude residue was purified by silica gel column chromatography (dichloromethane/methanol = 40/1), affording compound DDY01 (279 mg, 83%) as a white solid. Melting point: 189–190 °C. IR (neat) νmax 3038, 1650, 1523, 1328, 1159, 935, 841, 704 cm−1. 1H NMR (400 MHz, DMSO-d6) δ 12.57 (s, 1H), 10.13 (s, 1H), 8.63 (t, J = 5.7 Hz, 1H), 8.58 (d, J = 2.2 Hz, 1H), 8.48 (d, J = 3.1 Hz, 1H), 8.27 (d, J = 7.5 Hz, 1H), 7.97–7.90 (m, 1H), 7.91–7.79 (m, 4H), 7.77 (d, J = 7.9 Hz, 1H), 7.69–7.62 (m, 2H), 7.47–7.35 (m, 2H), 7.31 (d, J = 6.5 Hz, 1H), 7.23–7.15 (m, 1H), 4.79 (d, J = 5.6 Hz, 2H), 4.29 (s, 2H), 3.70 (t, J = 5.2 Hz, 2H), 3.26 (d, J = 5.3 Hz, 2H), 2.97 (d, J = 5.4 Hz, 2H), 2.83 (d, J = 4.5 Hz, 2H). 13C NMR (101 MHz, DMSO-d6) δ 181.18, 164.40, 159.85, 156.76 (d, J = 244.4 Hz), 149.42, 148.69, 145.28, 144.69, 135.76, 135.30 (d, J = 3.3 Hz), 134.61, 133.94, 132.35, 132.27, 132.02, 129.55, 129.17, 128.84, 128.35, 126.53, 125.90, 123.90, 123.62 (d, J = 18.2 Hz), 121.91, 116.33 (d, J = 21.6 Hz), 46.10, 45.18, 41.04, 36.85. HRMS (ESI) m/z calculated for C33H30FN7O4S2 [M + H]+ 672.1857, found 672.1858.

1-(4-((4-(2-fluoro-5-((4-oxo-3,4-dihydrophthalazin-1-yl)methyl)benzoyl)piperazin-1-yl)sulfonyl)phenyl)-3-(pyridin-3-ylmethyl)urea (compound DDY02)

Compound DDY02 was synthesized using compound 29 as a key intermediate, following a procedure similar to that employed for the synthesis of compound DDY01. White solid; yield: 33%; melting point: 197–198 °C. IR (neat) νmax 2988, 2905, 1698, 1645, 1538, 1151, 837, 721 cm^{-1}. ^{1}H NMR (400 MHz, DMSO-d_6) δ 12.57 (s, 1H), 9.28 (s, 1H), 8.56 (d, J = 2.2 Hz, 1H), 8.48 (d, J = 3.2 Hz, 1H), 8.34–8.23 (m, 1H), 7.97–7.91 (m, 1H), 7.90–7.80 (m, 2H), 7.76 (d, J = 7.9 Hz, 1H), 7.70–7.64 (m, 2H), 7.63–7.56 (m, 2H), 7.46–7.35 (m, 2H), 7.32 (d, J = 6.5 Hz, 1H), 7.19 (t, J = 9.0 Hz, 1H), 6.98 (t, J = 6.0 Hz, 1H), 4.36 (d, J = 5.9 Hz, 2H), 4.30 (s, 2H), 3.70 (t, J = 5.1 Hz, 2H), 3.26 (t, J = 5.0 Hz, 2H), 2.93 (t, J = 5.2 Hz, 2H), 2.80 (t, J = 5.1 Hz, 2H). ^{13}C NMR (101 MHz, DMSO-d_6) δ 164.38, 159.84, 156.75 (d, J = 244.7 Hz), 155.30, 148.79, 148.18, 145.53, 145.28, 136.24, 135.92, 135.31, 133.92, 132.29 (d, J = 8.4 Hz), 132.02, 129.55, 129.32, 128.35, 126.57, 126.53, 125.90, 124.09, 123.73, 123.55, 117.78, 116.31 (d, J = 21.5 Hz), 49.07, 46.11, 40.96, 36.84. HRMS (ESI) m/z calculated for $C_{33}H_{30}FN_7O_5S$ $[M + H]^+$ 656.2086, found 656.2087.

1-(4-((4-(3-(4-oxo-3,4-dihydroquinazolin-2-yl)propanoyl)piperazin-1-yl)sulfonyl)phenyl)-3-(pyridin-3-ylmethyl)urea (compound DDY03)

Compound DDY03 was synthesized using compound 29 as a key intermediate, following a procedure similar to that employed for the synthesis of compound DDY01. White solid; yield: 55%; melting point: 120–121 °C. IR (neat) νmax 2979, 2893, 1707, 1668, 1618, 1538, 1159, 940, 781, 730 cm^{-1}. ^{1}H NMR (400 MHz, DMSO-d_6) δ 12.12 (s, 1H), 9.42 (s, 1H), 8.55 (s, 1H), 8.47 (d, J = 3.2 Hz, 1H), 8.04 (d, J = 9.5 Hz, 1H), 7.76–7.65 (m, 4H), 7.60 (d, J = 8.6 Hz, 2H), 7.42–7.32 (m, 2H), 7.29 (d, J = 8.1 Hz, 1H), 7.06 (t, J = 6.0 Hz, 1H), 4.36 (d, J = 5.9 Hz, 2H), 3.69–3.59 (m, 2H), 3.53 (t, J = 5.2 Hz, 2H), 2.92 (t, J = 4.8 Hz, 2H), 2.84–2.71 (m, 6H). ^{13}C NMR (101 MHz, DMSO-d_6) δ 170.05, 162.02, 157.16, 155.34, 149.19, 149.12, 148.55, 145.57, 136.04, 135.43, 134.65, 129.37, 126.99, 126.35, 126.27, 126.13, 123.92, 121.29, 117.64, 46.62, 46.34, 44.70, 29.82, 28.76. HRMS (ESI) m/z calculated for $C_{28}H_{29}N_7O_5S$ $[M + H]^+$ 576.2024, found 576.2022.

2-((4-Fluoro-3-(4-((4-(3-(pyridin-3-ylmethyl)thioureido)phenyl)sulfonyl)piperazine-1-carbonyl)benzyl)oxy)benzamide (compound DDY04)

Compound DDY04 was synthesized using compound 28 as a key intermediate, following a procedure similar to that employed for the synthesis of compound DDY01. White solid; yield: 86%; melting point: 125–126 °C. IR (neat) νmax 3032, 1650, 1541, 1319, 1224, 1156, 940, 831, 710 cm^{-1}. ^{1}H NMR (400 MHz, DMSO-d_6) δ 10.42 (s, 1H), 8.85 (s, 1H), 8.57 (s, 1H), 8.47 (d, J = 3.3 Hz, 1H), 7.87 (d, J = 8.6 Hz, 2H), 7.75 (d, J = 5.9 Hz, 2H), 7.66 (d, J = 8.7 Hz,

2H), 7.64–7.60 (m, 1H), 7.55 (s, 1H), 7.53–7.48 (m, 1H), 7.46–7.40 (m, 1H), 7.37 (d, J = 7.8, 4.8 Hz, 1H), 7.32 (t, J = 9.0 Hz, 1H), 7.16 (d, J = 8.3 Hz, 1H), 7.03 (t, J = 7.5 Hz, 1H), 5.21 (s, 2H), 4.80 (s, 2H), 3.74 (t, J = 5.1 Hz, 2H), 3.33 (s, 2H), 2.99 (t, J = 5.0 Hz, 2H), 2.88 (t, J = 5.1 Hz, 2H). ^{13}C NMR (101 MHz, DMSO-d_6) δ 181.16, 167.04, 164.23, 157.67 (d, J = 246.3 Hz), 156.27, 149.42, 148.69, 144.69, 135.76, 134.61, 133.95 (d, J = 3.2 Hz), 132.57, 131.63 (d, J = 8.3 Hz), 131.01, 129.10, 128.87, 127.80, 124.34, 123.91, 123.75, 121.91, 121.33, 116.57 (d, J = 21.8 Hz), 113.94, 69.34, 46.50, 46.33, 46.16. HRMS (ESI) m/z calculated for $C_{32}H_{31}FN_6O_6S_2$ $[M + H]^+$ 663.1854, found 663.1865.

2-((4-fluoro-3-(4-((4-(3-(pyridin-3-ylmethyl)ureido)phenyl)sulfonyl)piperazine-1-carbonyl)benzyl)oxy)benzamide (compound DDY05)

Compound DDY05 was synthesized using compound 29 as a key intermediate, following a procedure similar to that employed for the synthesis of compound DDY01. White solid; yield: 81%; melting point: 119–120 °C. IR (neat) νmax 3401, 1650, 1535, 1221, 1156, 1100, 940, 834, 730 cm^{-1}. ^{1}H NMR (400 MHz, DMSO-d_6) δ 9.26 (s, 1H), 8.64–8.44 (m, 2H), 7.74 (t, J = 7.1 Hz, 2H), 7.63 (d, J = 16.6 Hz, 5H), 7.57–7.46 (m, 3H), 7.47–7.35 (m, 2H), 7.31 (t, J = 8.9 Hz, 1H), 7.17 (d, J = 8.2 Hz, 1H), 7.04 (t, J = 7.5 Hz, 1H), 6.96 (d, J = 6.2 Hz, 1H), 5.21 (s, 2H), 4.35 (d, J = 5.8 Hz, 2H), 3.73 (s, 2H), 3.42 (s, 2H), 2.95 (s, 2H), 2.84 (s, 2H). ^{13}C NMR (101 MHz, DMSO-d_6) δ 167.03, 164.21, 157.67 (d, J = 246.2 Hz), 156.28, 155.28, 148.97, 148.35, 145.54, 136.14, 135.72, 133.95 (d, J = 3.2 Hz), 132.55, 131.61 (d, J = 8.5 Hz), 131.01, 129.34, 128.92, 126.56, 124.36, 124.03, 123.87 (d, J = 18.2 Hz), 121.33, 117.79, 116.55 (d, J = 21.9 Hz), 113.95, 69.37, 46.50, 46.31, 46.16. HRMS (ESI) m/z calculated for $C_{32}H_{31}FN_6O_6S$ $[M + H]^+$ 647.2083, found 647.2078.

2-((4-fluoro-3-(4-((4-(3-(pyridin-3-ylmethyl)ureido)benzyl)sulfonyl)piperazine-1-carbonyl)benzyl)oxy)benzamide (compound DDY06)

Compound DDY06 was synthesized using compound 30 as a key intermediate, following a procedure similar to that employed for the synthesis of compound DDY01. White solid; yield: 37%; melting point: 146–147 °C. IR (neat) νmax 3039, 1647, 1544, 1511, 1313, 1226, 1150, 943, 840, 754 cm^{-1}. ^{1}H NMR (400 MHz, DMSO-d_6) δ 8.73 (s, 1H), 8.53 (d, J = 2.2 Hz, 1H), 8.45 (d, J = 3.0 Hz, 1H), 7.75 (d, J = 5.8 Hz, 1H), 7.71 (d, J = 7.8 Hz, 1H), 7.65 (t, J = 8.0 Hz, 1H), 7.59 (s, 1H), 7.55 (d, J = 6.5 Hz, 2H), 7.45–7.40 (m, 3H), 7.38–7.31 (m, 2H), 7.26 (d, J = 8.6 Hz, 2H), 7.19 (d, J = 8.3 Hz, 1H), 7.04 (t, J = 7.3 Hz, 1H), 6.75 (t, J = 6.0 Hz, 1H), 5.26 (s, 2H), 4.42–4.26 (m, 4H), 3.67 (t, J = 5.2 Hz, 2H), 3.21 (d, J = 15.3 Hz, 4H), 3.08 (s, 2H). ^{13}C NMR (101 MHz, DMSO-d_6) δ 167.13, 164.32, 157.70 (d, J = 246.2 Hz), 156.23, 155.64, 149.20, 148.50, 140.97, 136.29, 135.46, 134.00, 132.55, 131.75, 131.54 (d, J = 8.1 Hz), 130.98, 128.64, 124.47, 124.06 (d, J = 18.4 Hz), 123.92, 121.89, 121.34, 118.01, 116.64 (d, J = 21.9 Hz), 113.94, 69.32, 55.38, 47.02, 46.08, 45.76. HRMS (ESI) m/z calculated for $C_{33}H_{33}FN_6O_6S$ $[M + H]^+$ 661.2239, found 661.2234.

5-fluoro-2-((4-fluoro-3-(4-((4-(3-(pyridin-3-ylmethyl)ureido)phenyl)sulfonyl)piperazine-1-carbonyl)benzyl)oxy)benzamide (compound DDY07)

Compound DDY07 was synthesized using compound 29 as a key intermediate, following a procedure similar to that employed for the synthesis of compound DDY01. White solid; yield: 76%; melting point: 122–123 °C. IR (neat) νmax 3420, 3174, 1644, 1544, 1434, 1233, 1156, 926, 828, 727 cm^{-1}. ^{1}H NMR (400 MHz, DMSO-d_6) δ 9.23 (s, 1H), 8.54 (d, J = 2.2 Hz, 1H), 8.46 (d, J = 4.8 Hz, 1H), 7.72 (d, J = 7.8 Hz, 1H), 7.69–7.63 (m, 4H), 7.60 (d, J = 8.9 Hz, 3H), 7.52–7.46 (m, 2H), 7.38–7.34 (m, 1H), 7.34–7.30 (m, 1H), 7.30–7.27 (m, 1H), 7.21 (d, J = 4.4 Hz, 1H), 6.94 (t, J = 6.0 Hz, 1H), 5.20 (s, 2H), 4.35 (d, J = 5.9 Hz, 2H), 3.73 (t, J = 5.2 Hz, 2H), 3.30 (t, J = 5.0 Hz, 2H), 2.95 (t, J = 5.1 Hz, 2H), 2.84 (s, 2H). ^{13}C NMR (101 MHz, DMSO-d_6) δ 165.79, 164.18, 157.69 (d, J = 246.3 Hz), 156.63 (d, J = 237.6 Hz), 155.26, 152.58 (d, J = 2.0 Hz), 149.19, 148.56, 145.55, 136.01, 135.46, 133.77 (d, J = 3.4 Hz), 131.66 (d, J = 8.2 Hz), 129.34, 128.97, 126.50, 125.96 (d, J = 6.5 Hz), 123.93, 123.88 (d, J = 18.4 Hz), 118.79 (d, J = 23.1 Hz), 117.78, 116.93 (d, J = 24.4 Hz), 116.56 (d, J = 22.0 Hz), 115.93 (d, J = 7.8 Hz), 70.04, 46.49, 46.16, 40.98. HRMS (ESI) m/z calculated for $C_{32}H_{39}F_2N_6O_6S$ $[M + H]^+$ 665.1988, found 665.1984.

2-((3-(4-((4-(3-(pyridin-3-ylmethyl)ureido)phenyl)sulfonyl)piperazine-1-carbonyl)benzyl)oxy)benzamide (compound DDY08)

Compound DDY08 was synthesized using compound 29 as a key intermediate, following a procedure similar to that employed for the synthesis of compound DDY01. White solid; yield: 81%; melting point: 202–203 °C. IR (neat) νmax 3325, 3041, 1698, 1647, 1588, 1538, 1213, 1153, 1106, 937, 831, 730 cm^{-1}. ^{1}H NMR (400 MHz, DMSO-d_6) δ 9.22 (s, 1H), 8.54 (d, J = 2.2 Hz, 1H), 8.46 (d, J = 3.1 Hz, 1H), 7.77 (d, J = 7.7 Hz, 1H), 7.75–7.68 (m, 1H), 7.69–7.62 (m, 2H), 7.63–7.54 (m, 4H), 7.54–7.49 (m, 1H), 7.47 (d, J = 2.4 Hz, 1H), 7.48–7.39 (m, 2H), 7.40–7.33 (m, 1H), 7.36–7.29 (m, 1H), 7.17 (d, J = 8.8 Hz, 1H), 7.07–6.99 (m, 1H), 6.94 (t, J = 6.0 Hz, 1H), 5.26 (s, 2H), 4.35 (d, J = 5.8 Hz, 2H), 3.69 (s, 2H), 3.46 (s, 2H), 2.90 (s, 4H). ^{13}C NMR (101 MHz, DMSO-d_6) δ 169.38, 167.00, 156.38, 155.28, 149.17, 148.54, 145.49, 137.38, 136.04, 135.92, 135.47, 132.61, 131.06, 129.48, 129.34, 129.22, 127.33, 126.75, 126.64, 124.16, 123.94, 121.26, 117.79, 113.89, 69.94,

55.39, 46.22, 40.98. HRMS (ESI) m/z calculated for $C_{32}H_{32}N_6O_6S$ $[M + H]^+$ 629.2177, found 629.2176.

5-fluoro-2-((3-(4-((4-(3-(pyridin-3-ylmethyl)ureido)phenyl)sulfonyl)piperazine-1-carbonyl)benzyl)oxy)benzamide (compound DDY09)

Compound DDY09 was synthesized using compound 29 as a key intermediate, following a procedure similar to that employed for the synthesis of compound DDY01. White solid; yield: 78%; melting point: 147–148 °C. IR (neat) νmax 3423, 3062, 1665, 1428, 1260, 1159, 822, 727 cm^{-1}. ^1H NMR (400 MHz, DMSO-d_6) δ 9.22 (s, 1H), 8.54 (d, J = 2.2 Hz, 1H), 8.46 (d, J = 6.4 Hz, 1H), 7.71 (d, J = 7.9 Hz, 1H), 7.69–7.63 (m, 4H), 7.59 (d, J = 9.0 Hz, 2H), 7.58–7.54 (m, 1H), 7.51 (d, J = 6.0 Hz, 1H), 7.48–7.42 (m, 2H), 7.39–7.34 (m, 1H), 7.34–7.27 (m, 2H), 7.22 (d, J = 4.3 Hz, 1H), 6.93 (t, J = 6.0 Hz, 1H),5.24 (s, 2H), 4.35 (d, J = 5.9 Hz, 2H), 3.78–3.57 (m, 2H), 3.40 (s, 2H), 3.00–2.83 (m, 4H). ^{13}C NMR (101 MHz, DMSO-d_6) δ 169.37, 165.75, 162.78, 156.59 (d, J = 237.4 Hz), 155.27, 152.69 (d, J = 1.9 Hz), 149.19, 148.56, 145.50, 137.21, 135.98 (d, J = 8.3 Hz), 135.45, 129.51, 129.33, 129.23, 127.39, 126.79, 126.65, 125.77 (d, J = 6.5 Hz), 123.93, 118.85 (d, J = 23.0 Hz), 117.79, 116.96 (d, J = 24.4 Hz), 115.85 (d, J = 7.8 Hz), 70.62, 46.85, 46.23, 40.98. HRMS (ESI) m/z calculated for $C_{32}H_{31}FN_6O_6S$ $[M + H]^+$ 647.2083, found 647.2074.

2-(4-((4-(3-(pyridin-3-ylmethyl)thioureido)phenyl)sulfonyl)piperazine-1-carbonyl)-1H-benzo[d]imidazole-4-carboxamide (compound DDY10)

Compound DDY10 was synthesized using compound 28 as a key intermediate, following a procedure similar to that employed for the synthesis of compound DDY01. Yellow solid; yield: 23%; melting point: >250 °C. IR (neat) νmax 3304, 3227, 1671, 1621, 1494, 1423, 1307, 1239, 1165, 937, 739 cm^{-1}. ^1H NMR (400 MHz, DMSO-d_6) δ 13.58 (s, 1H), 10.12 (s, 1H), 8.68 (s, 1H), 8.64–8.59 (m, 1H), 8.57 (d, J = 2.2 Hz, 1H), 8.48 (d, J = 4.8 Hz, 1H), 7.93 (d, J = 7.3 Hz, 1H), 7.81 (d, J = 8.7 Hz, 2H), 7.77 (d, J = 5.8 Hz, 2H), 7.69 (d, J = 8.7 Hz, 3H), 7.44 (t, J = 7.6 Hz, 1H), 7.38 (dd, J = 7.9, 4.7 Hz, 1H), 4.78 (d, J = 5.6 Hz, 2H), 4.36 (s, 2H), 3.83 (s, 2H), 3.21–2.94 (m, 4H). ^{13}C NMR (151 MHz, DMSO-d_6) δ 181.14, 166.02, 158.54, 149.27, 148.55, 145.77, 144.63, 140.10, 135.90, 134.68, 134.08, 128.93, 124.52, 124.43, 124.25, 123.95, 121.94, 118.87, 116.49, 46.72, 46.20, 45.18. HRMS (ESI) m/z calculated for $C_{26}H_{26}N_8O_4S_2$ $[M + H]^+$ 579.1591, found 579.1596.

2-(4-((4-(3-(pyridin-3-ylmethyl)ureido)phenyl)sulfonyl)piperazine-1-carbonyl)-1H-benzo[d]imidazole-4-carboxamide (compound DDY11)

Compound DDY11 was synthesized using compound 29 as a key intermediate, following a procedure similar to that employed for the synthesis of compound DDY01. Yellow solid; yield: 41%; melting point: >250 °C. IR (neat) νmax 3479, 3242, 1668, 1624, 1585, 1494, 1245, 1159, 937, 733 cm^{-1}. ^1H NMR (400 MHz, DMSO-d_6) δ 13.57 (s, 1H), 9.24 (s, 1H), 8.68 (s, 1H), 8.61–8.49 (m, 1H), 8.46 (d, J = 4.8 Hz, 1H), 7.92 (d, J = 7.5 Hz, 1H), 7.73 (d, J = 8.2 Hz, 3H), 7.63 (q, J = 8.8 Hz, 4H), 7.43 (s, 1H), 7.41–7.33 (m, 1H), 6.93 (t, J = 6.1 Hz, 1H), 4.34 (d, J = 6.0 Hz, 4H), 3.81 (s, 2H), 3.02 (s, 4H). ^{13}C NMR (101 MHz, DMSO-d_6) δ 166.04, 158.54, 155.27, 148.89, 148.28, 145.80, 145.54, 140.11, 136.17, 135.77, 134.09, 129.38, 126.39, 124.46, 124.23, 124.04, 117.77, 116.50, 46.69, 46.18, 42.11. HRMS (ESI) m/z calculated for $C_{26}H_{26}N_8O_5S$ $[M + H]^+$ 563.1820, found 563.1838.

Molecule docking

From the Protein Data Bank, the solved structures of NAMPT (PDB ID: 4JR5) and PARP1 (PDB ID: 5DS3) were downloaded. The docking experiments were carried out using the BIOVIA Discovery Studio 2016 software package (San Diego, CA, USA). Preparation of both protein models was accomplished with the Protein Preparation module. For PARP1, all parameters were left at their factory defaults. The handling of NAMPT differed in one respect: the "Keep Water" option was set to "selected," preserving some structurally conserved water molecules within the model. The active-site search space was specified as a spherical volume with a 15 Å radius, the center of which was defined by the position of the bound ligand through the From Current Selection function.

Conformational energy minimization of the docked species was performed under the CHARMm forcefield via the Full Minimization module. Actual docking runs were then executed using the CDOCKER engine, with "Pose Cluster Radius" fixed at 0.5 and "Orientations to Refine" set to 20. The ten highest-ranked solutions were collected for each ligand, and the single pose judged to have the optimal interaction network was carried forward for binding-mode deconstruction with the "Display receptor-ligand interactions" tool. All structural images were generated in PyMol (version 2.5).

Determination of inhibition rates and IC50 values against NAMPT and PARP1

Enzymatic profiling against NAMPT and PARP1 was contracted to Huawei Pharmaceutical Co., Ltd. (Jinan, China). Compound stocks were prepared at 10× the desired final strength in 10% DMSO; 5 μL of each stock was then combined with 45 μL of reaction master mix, yielding a uniform DMSO background of 1%. All reactions were assembled in duplicate and incubated at 30 °C for 90 min. The 50 μL reaction volume contained 50

mM Tris-HCl (pH 8.0), 12.5 mM MgCl2, 20 μM nicotinamide, 0.4 mM phosphoribosyl pyrophosphate, 2 mM ATP, 30 μg/mL alcohol dehydrogenase, 10 μg/mL NMNAT, 1.5% alcohol, 1 mM DTT, 0.02% BSA, 0.01% Tween 20, and the inhibitor being tested. Fluorescence was measured with excitation at 360 nm and emission at 460 nm on a Tecan Infinite M1000 microplate reader. NAMPT assays were performed in duplicate at each inhibitor concentration. Data processing was handled in GraphPad Prism software (version 8.3.0). The fluorescence intensity recorded in inhibitor-free wells (Ft) was taken to correspond to 100% activity; the signal from wells lacking NAMPT (Fb) was set as the 0% activity baseline. Percent activity remaining in the presence of an inhibitor was obtained from the expression %activity = (F − Fb)/(Ft − Fb), where F is the fluorescence intensity of the inhibitor-containing well. In keeping with this procedure, DDY01–DDY11 were first evaluated for NAMPT blockade at a test concentration of 0.1 μM. A subset of compounds was then taken through a nine-point dilution series (0.01 nM, 0.03 nM, 0.1 nM, 0.33 nM, 1 nM, 3.3 nM, 10 nM, 33 nM, 100 nM) to establish full concentration–effect relationships. IC50 values were derived by non-linear regression curve fitting in GraphPad Prism.

PARP1 catalytic activity was assessed using an ELISA protocol adapted to 96-well plates. Histone (20 μg/mL in 100 μL PBS) was adsorbed to each well by incubation at 4 °C overnight. The following day, a 30 μL mixture of NAD+ (100 μM), biotinylated NAD+ (25 μM), and slDNA (200 nM) in reaction buffer (2 mM MgCl2, 50 mM Tris, pH 8.0) was dispensed into the coated wells. A 5 μL volume of inhibitor solution or vehicle was then added. The reaction was initiated by adding 20 μL of PARP1 (50 ng/well), and the plate was incubated at 30 °C for 1 h. After this incubation, 50 μL of streptavidin-linked HRP was added, and the plate was incubated at 30 °C for an additional 30 min. The signal was generated by adding 100 μL of a chemiluminescent substrate mixture (H2O2 and luminol in 0.1 M citrate buffer, pH 5.4), and luminescence was measured on a SpectraMax M5 microplate reader (Molecular Devices™, San Jose, CA, USA). The degree of PARP1 inhibition was expressed as (Lu control − Lu treated)/Lu control × 100%. IC50 values, defined as the concentration producing half-maximal enzyme inhibition, were computed by fitting normalized dose–response curves using non-linear regression in GraphPad Prism (version 8.3.0). An initial single-concentration screen of DDY01–DDY11 was run at 0.5 μM. Following this, detailed concentration–response profiles were recorded for selected candidates across the same nine-concentration range described above, and IC50 values were again extracted by non-linear regression in GraphPad Prism.

Cell culture

The cell lines MDA-MB-468, MDA-MB-231, MCF-7, and MCF-10A were procured from the National Collection of Authenticated Cell Culture, China. Cultures were grown in DMEM medium containing 10% FBS and 1% penicillin/streptomycin and incubated at 37 °C in a 5% CO2, humidified incubator.

Cell viability assay

The MTT assay was employed to gauge cell viability. Cells were seeded into 96-well plates at 3×10^3 cells per well and subsequently exposed to compounds at concentrations of 0.05, 0.2, 0.8, 3.2, 6.4, and 12.8 μM for 72 h. At the endpoint, 100 μL of MTT working solution (0.5 mg/mL) was introduced into each well. After a 4 h incubation period, the formazan crystals were dissolved in 150 μL DMSO, and absorbance was measured at 570 nm using a microplate reader.

Western blot analysis

For protein expression analysis, cells were treated with DDY02, FK866, or Olaparib for 24 h, after which lysis was performed with RIPA buffer containing protease and phosphatase inhibitors. Protein concentrations in the lysates were standardized using the BCA Protein Assay Kit (Thermo Fisher Scientific™, Waltham, MA, USA). Samples containing 20–30 μg of total protein were electrophoresed on SDS-polyacrylamide gels and blotted onto PVDF membranes. Non-specific binding sites were saturated with 5% milk in PBS. The membranes were then incubated with primary antibodies recognizing γ-H2AX (Cell Signaling Technology™, Danvers, MA, USA), BCL2 (Abcam™, Cambridge, UK), or β-actin (Proteintech™, Rosemont, IL, USA). Following an overnight incubation at 4 °C, the membranes were washed, exposed to HRP-conjugated secondary antibodies for 1 h, and developed with ECL reagent (Labgic TechnologyTM, Beijing, China).

Apoptosis assays

Detection of apoptotic cell populations relied on the Annexin V-FITC/PI dual-labeling kit manufactured by KeyGen Biotech (Nanjing, China). Into six-well plates, MDA-MB-468 cells were introduced at 5×10^5 cells/mL and subsequently challenged with the test compounds at the appropriate concentrations for 72 h. Harvested cells were then subjected to a 15 min staining step at room temperature in the dark, during which 5 μL each of Annexin V-FITC and PI was added. Event acquisition and analysis were accomplished on a BD Accuri C6 Plus flow cytometer (BD Bioscience, San Jose, CA, USA).

Clonogenic assay

The capacity of individual cells to form macroscopic colonies was examined by seeding MDA-MB-468 cells at low density (500 cells/well) in 6-well plates. Colonies were allowed to develop over a 7-day growth period. Once colonies had formed, the wells were gently washed with PBS, then the cells were fixed in methanol (15 min) and stained with 1% crystal violet for 1 h. Images of the stained wells were then captured, and the visible colonies were enumerated.

Cell migration assay

A wound-healing setup served to measure the migratory response. Briefly, 5×10^5 MDA-MB-468 cells were placed into each well of a 6-well plate and allowed to adhere overnight. The confluent monolayer was then disrupted by dragging a sterile 10 μL pipette tip across the surface to generate a linear cell-free gap. PBS washing cleared away loosened cells and debris. DDY02, FK866, or Olaparib was then introduced, and the movement of cells back into the denuded zone was tracked by acquiring images at the 0, 12, 24, and 48 h time marks.

Comet assay

Single-cell electrophoresis at alkaline pH was performed using the Beyotime Comet Assay Kit (Shanghai, China), and all steps were carried out exactly as specified in the accompanying manual. To summarize, after a 24 h incubation with DDY02, FK866, Olaparib, or the combined treatments, the cells were collected, mixed with 0.7% low-melting-point agarose at a 1:7 (v/v) ratio, and promptly spread onto glass slides. The slides were then submerged in lysis solution for 1 h. Electrophoretic migration of DNA was driven at 25 V and 300 mA using a horizontal apparatus. DNA was rendered visible by PI staining, and the resulting comets were imaged under a fluorescence inverted microscope.

NAD level determination assay

Quantification of the intracellular NAD pool was performed using the NAD+/NADH Assay kit with the WST-8 detection system (Beyotime, China); the manufacturer's instructions were followed without deviation. Centrifugation-harvested cells were lysed in the provided NAD+/NADH extraction buffer. The resulting lysate was combined with the acetaldehyde dehydrogenase working solution, incubated at 37 °C for 10 min, and then mixed with the colorimetric developing reagent. Absorbance read at 450 nm furnished the total NADH plus NAD+ concentration. For the separate quantitation of NADH alone, an aliquot of lysate was preheated to 60 °C for 30 min before the acetaldehyde dehydrogenase working solution was added. The net NAD+ level was then obtained from the arithmetic difference: [NAD+] = [NADH + NAD+] − [NADH].

Results and Discussion

Design

As shown in **Figure 3a**, Zheng *et al*. [26] identified compound 11, a thiourea derivative, as a high-potency NAMPT inhibitor. The crystallographic analysis of its co-complex with NAMPT was determined by X-ray diffraction (PDB ID: 4JR5). In a subsequent effort, an unaffiliated team under Sheng generated 46 structural descendants of 11, encompassing compounds 12-14, and performed an exhaustive structure–activity relationship characterization [27]. The cumulative data indicated that chemical modifications introduced at the distal nitrogen of the piperazine ring in 12 were well accepted, without eroding NAMPT inhibitory activity. **Figure 3b** captured the docking-derived binding posture of 12 within NAMPT. Crucially, the piperazine substructure was found to protrude into the solvent-channel region, implying that the installation of additional elements onto this piperazine would not detract from NAMPT engagement.

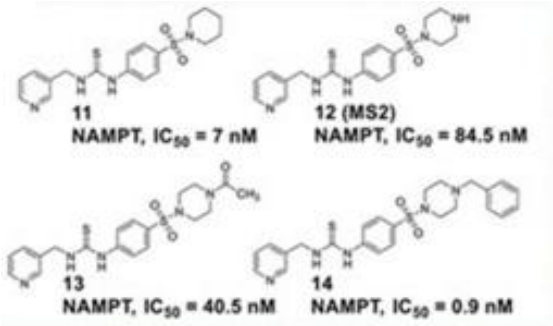

a)

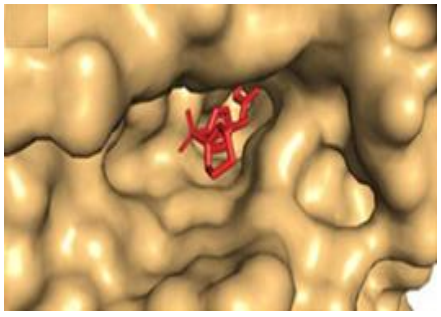

b)

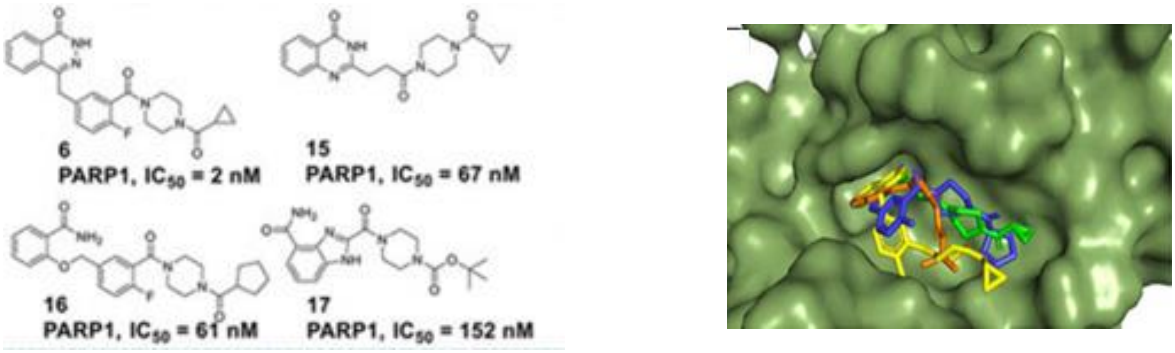

Figure 3. The modeled poses of NAMPT inhibitors and PARP1 inhibitors in the binding site: (a) The structures of NAMPT inhibitors; (b) the modeled pose of NAMPT inhibitor 11 (red) in the binding site of NAMPT; (c) the structures of PARP1 inhibitors; (d) the modeled poses of PARP1 inhibitors 6 (yellow), 15 (green), 16 (blue), and 17 (orange) in the binding site of PARP1.

Leveraging these structural clues, Sheng's laboratory used 12 and its analogs as starting points for assembling multifunctional ligands targeting NAMPT. This versatile strategy gave rise to dual-target inhibitors, proteolysis-targeting chimeras (PROTACs), and fluorescent reporters, underscoring the broad applicability of these chemotypes in NAMPT-oriented discovery [28-33].

As illustrated in **Figure 3c**, compounds 6 and 15~17 together define a family of PARP1 inhibitors that incorporate a piperazine connector [22-25, 34]. As visualized in **Figure 3d**, docking simulations interrogating their interaction with PARP1 disclosed that the piperazine units in this series form an amide bridge linking the PARP1 recognition motif, tethering the ligand within the active-site pocket, whereas the pendant group on the piperazine ring extends away into the surrounding solvent. Given the compatible binding topologies and favorable chemistry, the piperazine scaffold surfaced as a natural linker for pharmacophore fusion, enabling the merger of 12 with compounds 6 and 15~17. Informed by these considerations, as rendered in **Figure 4**, we borrowed the PARP1-binding pharmacophores from 6 and 15~17 (denoted by the blue segments). We grafted them onto the 12-framework, thereby obtaining a curated set of NAMPT/PARP1 dual-target inhibitors, which we named DDY01~DDY11.

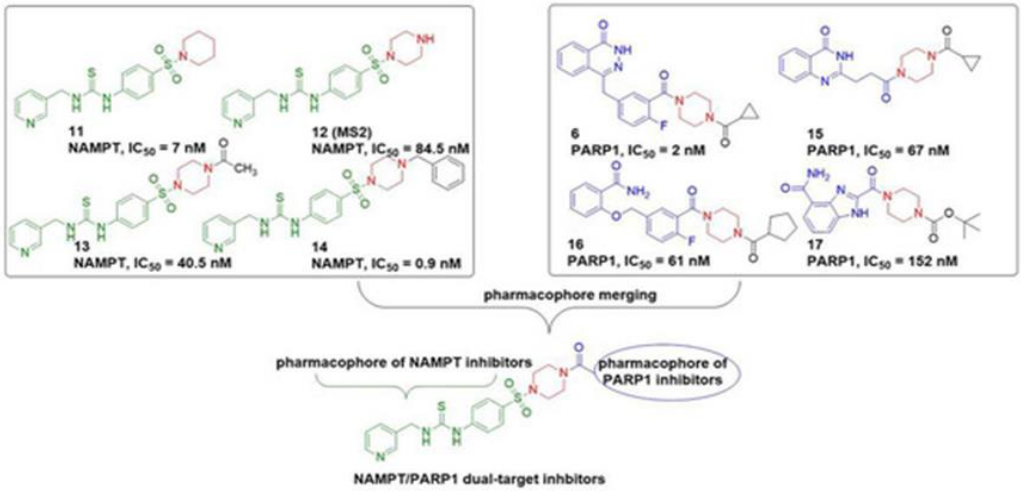

Figure 4. The design strategy of NAMPT/PARP1 dual-target inhibitors. The pharmacophores of NAMPT inhibitors and PARP1 inhibitors are shown in green and blue, respectively.

Biological screening

Enzymatic activities against NAMPT and PARP1

Compiled in **Table 1** are the inhibitory signatures recorded for the panel of eleven target compounds when profiled against both NAMPT and PARP1. A preliminary single-concentration survey was first conducted to gauge each molecule's capacity to blunt the catalytic function of the two enzymes. Only those candidates that crossed a meaningful inhibition threshold were advanced to full dose–response IC50 characterization, since weakly acting compounds would contribute little to validating the

premise of dual-target synergy. The hybrid molecule DDY01, which combines the pharmacophore blueprint of Olaparib (compound 6) with that of compound 12, suppressed NAMPT activity by 83% at a test concentration of 0.1 μM. However, its action on PARP1 decreased considerably, with an IC50 of 0.009 μM—a 4.5-fold drop compared with the parent Olaparib (IC50 = 0.002 μM). Swapping the thiourea linkage for a urea via bioisosteric design yielded DDY02, which showed a commendable NAMPT blockade (IC50 = 0.01 μM) but showed an incremental weakening in PARP1 inhibition, trailing DDY01 itself by an additional factor of 5.5. Another chimera, DDY03, assembled by splicing the pharmacophoric elements of compound 12 onto compound 15, eclipsed both progenitors, achieving IC50 values of 0.055 μM toward NAMPT and 0.025 μM toward PARP1. The subset DDY04 through DDY09, each embedding the pharmacophore of compound 16 tethered to the 12 scaffold, was subsequently evaluated. The thiourea-bearing DDY04 and its urea analog DDY05 each delivered strong NAMPT suppression at low exposure (84%–86% at 0.1 μM) while moderating PARP1 activity to a respectable degree. In a noteworthy shift, the homolog DDY06, which differs from DDY05 only by the insertion of a methylene linker between the benzene ring and the sulfonyl anchor, saw PARP1 inhibition climb to 89% at 0.5 μM. Still, its grip on NAMPT simultaneously slipped to a mere 48% at 0.1 μM. Seeking to reinforce PARP1 engagement further, we designed DDY07, DDY08, and DDY09, which explore incremental fluorination of the aromatic ring—an operational maneuver cited in earlier work as beneficial for PARP1 affinity [22]. Consistent with expectation, these fluorine additions lifted PARP1 inhibitory activity while sparing NAMPT potency. The final pair, DDY10 and DDY11, shares a benzimidazole core drawn from compound 17 but diverges sharply in outcome. The thiourea DDY10 was essentially inactive against NAMPT (7% at 0.1 μM) and showed only partial PARP1 inhibition (55% at 0.5 μM). In dramatic contrast, the urea counterpart DDY11 delivered robust dual inhibition, achieving IC50 values of 0.034 μM for NAMPT and 0.014 μM for PARP1, thereby satisfying the sought-after equilibrium in on-target potency.

Table 1. The inhibitory activities of target compounds against NAMPT and PARP1.

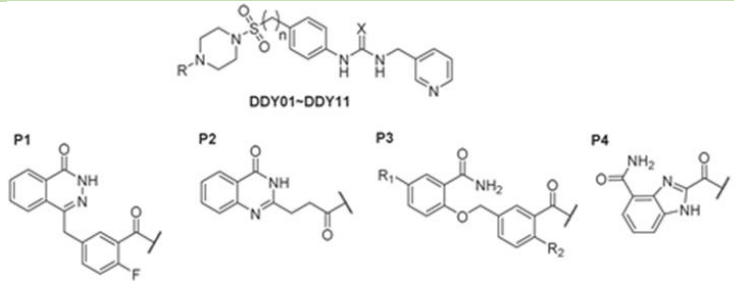

Compound	R	X	n	R_1	R_2	PARP1 IC_{50} (μM) [a] or inhibition rate (0.5 μM, %) [b]	NAMPT IC_{50} (μM) [a] or inhibition rate (0.1 μM, %) [b]
FK866	—	—	—	—	—	—	0.012 ± 0.004
Olaparib	—	—	—	—	—	0.002 ± 0.001	—
DDY01	P1	S	0	—	—	0.009 ± 0.002	83%
DDY02	P1	O	0	—	—	0.050 ± 0.010	0.010 ± 0.003
DDY03	P2	O	0	—	—	0.025 ± 0.007	0.055 ± 0.019
DDY04	P3	S	0	H	F	70%	84%
DDY05	P3	O	0	H	F	1.879 ± 0.600	86%
DDY06	P3	O	1	H	F	89%	48%
DDY07	P3	O	0	F	F	92%	84%
DDY08	P3	O	0	H	H	69%	80%
DDY09	P3	O	0	F	H	78%	86%
DDY10	P4	S	0	—	—	55%	7%
DDY11	P4	O	0	—	—	0.014 ± 0.003	0.034 ± 0.009

[a]: IC50 values are the mean of at least two independent experiments performed in duplicate with standard deviation. [b]: Inhibition rates were tested in duplicate; the average values were obtained.

Molecular docking study

Because DDY02 and DDY11 each struck an attractive balance between NAMPT and PARP1 blockade, they were singled out for a more granular examination of their predicted binding topologies via molecular docking.

Turning first to **Figures 5a and 5b**, the computed poses place DDY02 and 11 in near-identical orientations within the NAMPT active-site cavity. Both adopt a closely

matched interaction fingerprint. The pyridine nucleus is sandwiched between the aromatic side chains of Phe193 and TYR18′ through π–π stacking, while a hydrogen-bonding contact ties the urea carbonyl oxygen to the hydroxyl of Ser275. The sulfonyl oxygen and the urea NH, for their part, each reach out to engage structural water molecules. An additional conformational detail worth noting is the distal 4-benzyl phthalazinone appendage, which folds into a characteristic "J"-shaped arc, allowing it to establish optimally spaced contacts with the backbone atom of Gly305 and the side chain of Tyr188.

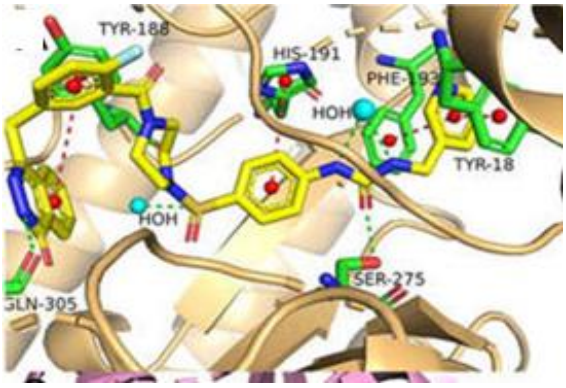

a)

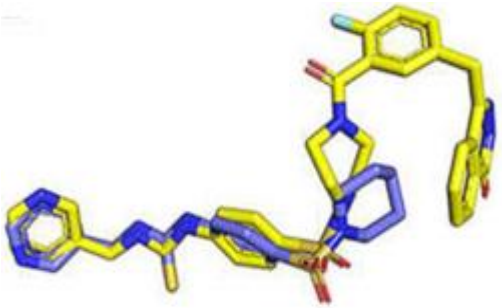

b)

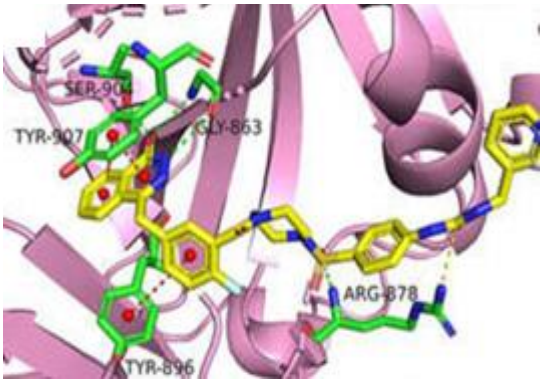

c)

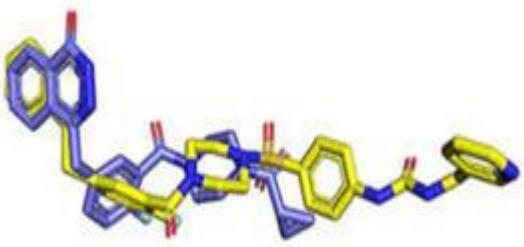

d)

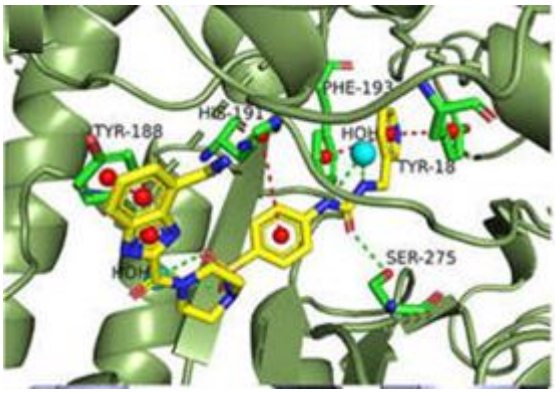

e)

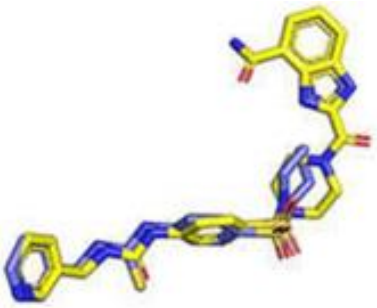

f)

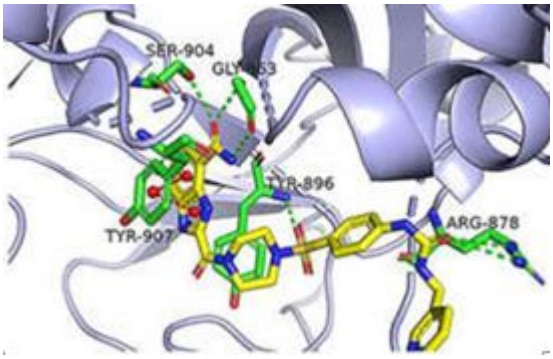

g)

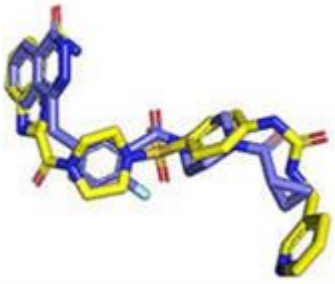

h)

Figure 5. Binding mode analysis of DDY02 and DDY11: (a) Binding mode of DDY02 with NAMPT (PDB ID: 4JR5), (b) Confirmation of DDY02 at the binding site of NAMPT, (c) Binding mode of DDY02 with PARP1 (PDB ID: 5DS3), (d) Confirmation of DDY02 at the binding site of PARP1, (e) Binding mode of DDY11 with NAMPT (PDB ID: 4JR5), (f) Confirmation of DDY11 at the binding site of NAMPT, (g) Binding mode of DDY11 with PARP1 (PDB ID: 5DS3), and (h) Confirmation of DDY11 at the binding site of PARP1. Hydrogen bonds are shown by green

dashed lines, and pi–pi stacking interactions are shown by red dashed lines. DDY02 and DDY11 are shown in yellow sticks; the ligands in the co-crystals are shown in purple sticks. The figure was generated using PyMol (version 2.5).

Looking next at **Figures 5c and 5d**, the manner in which DDY02 nestles into the PARP1 binding cleft broadly recapitulates the binding mode characteristic of Olaparib. The phthalazinone amide moiety anchors the pose through hydrogen bonds with Gly863 and Ser904, concurrent with π–π stacking of its aromatic rings against Tyr907 and Tyr896. Additional stabilizing contacts arise through hydrogen-bond donation from Arg878 to the sulfonyl and urea oxygen atoms. The terminal pyridine group, meanwhile, extends toward the solvent-exposed periphery of the pocket. A point of distinction between DDY02 and Olaparib deserves emphasis: rather than seamlessly overlaying the parent inhibitor, the fluorine-decorated benzene ring of DDY02 twists by approximately 90 degrees about its dihedral angle, reorienting to form a T-shaped edge-to-face π-interaction with Tyr896.

We likewise conducted docking for DDY11 in the binding cavities of both enzyme targets. The resulting models, depicted in **Figures 5e–5h**, indicate that DDY11, much like DDY02, assembles an ensemble of contacts—hydrogen bonds, van der Waals packing, π–π stacking, and hydrophobic clustering—with amino acid residues critical to the architecture of the NAMPT and PARP1 active sites. Considered in their entirety, the docking studies furnish a consistent picture: both DDY02 and DDY11 can effectively occupy the ligand-binding sites of NAMPT and PARP1, providing in silico corroboration of the conceptual foundation of our dual-target design platform.

Cytotoxicity assay

The growth-suppressive potency of the synthesized target compounds was benchmarked against FK866 and Olaparib, and their concomitant administration, across a panel of three breast cancer lines, with the resulting data collated in **Table 2**. Across all three models, FK866 alone proved considerably more growth-inhibitory than Olaparib. When the two agents were combined, the resulting anti-proliferative effect exceeded that of either drug alone, indicating a cooperative interaction. Stratifying by cell type, the triple-negative breast cancer (TNBC) representatives MDA-MB-231 and MDA-MB-468 exhibited greater vulnerability to FK866, Olaparib, and their pairing than did the MCF-7 line. Within our compound library, DDY10 emerged as the most potent suppressor of MDA-MB-231 expansion, eclipsing Olaparib yet not quite reaching the level of FK866. The vigorous cytostatic action of DDY10 in this line is noteworthy, given its minimal NAMPT-blocking properties, implying the involvement of alternative mechanistic pathways.

Among the synthesized analogs, DDY02 was the most effective agent for the MDA-MB-468 line. When tested in MCF-7 cells, DDY02, DDY06, and DDY11 showed roughly equivalent levels of growth attenuation; however, the molecules we prepared were, overall, less impactful against MCF-7 cultures than against either MDA-MB-468 or MDA-MB-231 cultures. This pattern dovetails with published observations from the Ashworth group, who reported a pronounced asymmetry in the synergistic pharmacodynamic interaction between NAMPT and PARP1 blockade when comparing MDA-MB-468 versus MDA-MB-231 cells [17]. Specifically, their investigation found that MDA-MB-468 cells responded far more vigorously to the FK866 plus Olaparib regimen than MDA-MB-231 cells. Guided by these collective findings, we selected the MDA-MB-468 line and our standout compound DDY02 for subsequent mechanistic interrogation.

Table 2. In vitro anti-proliferative activity of target compounds against breast cancer cell lines.

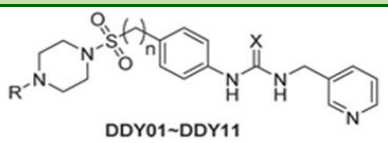

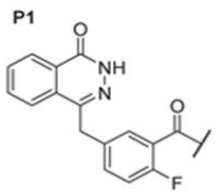

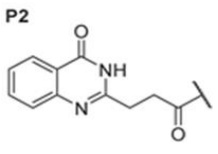

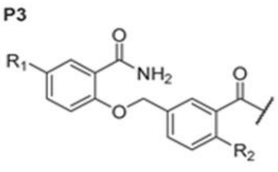

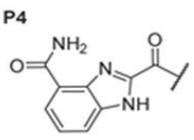

Compound	R	X	n	R1	R2	Cytotoxicity IC_{50} (μM) *		
						MCF-7	MDA-MB-468	MDA-MB-231
FK866	—	—	—	—	—	5.8 ± 0.86	4.01 ± 0.21	3.83 ± 0.12
Olaparib	—	—	—	—	—	8.68 ± 0.81	6.19 ± 0.09	6.74 ± 0.08

FK866 + Olaparib (1:1)	—	—	—	—	—	5.31 ± 0.03	3.59 ± 0.10	3.14 ± 0.09
DDY01	P1	S	0	—	—	8.48 ± 0.18	5.09 ± 0.09	6.17 ± 0.27
DDY02	P1	O	0	—	—	7.61 ± 0.14	4.43 ± 0.04	10.43 ± 0.16
DDY03	P2	O	0	—	—	11.23 ± 0.79	8.17 ± 0.31	10.88 ± 0.68
DDY04	P3	S	0	H	F	13.37 ± 2.41	14.06 ± 0.3	13.48 ± 0.66
DDY05	P3	O	0	H	F	>20	8.02 ± 0.74	10.22 ± 0.29
DDY06	P3	O	1	H	F	7.95 ± 0.34	17.16 ± 1.57	15.36 ± 2.15
DDY07	P3	O	0	F	F	13.47 ± 0.16	7.43 ± 0.23	8.1 ± 0.71
DDY08	P3	O	0	H	H	9.18 ± 0.44	12.89 ± 1.69	11.09 ± 0.19
DDY09	P3	O	0	F	H	11.01 ± 0.82	6.98 ± 0.57	8.7 ± 0.24
DDY10	P4	S	0	—	—	8.83 ± 0.31	6.74 ± 0.16	4.45 ± 0.29
DDY11	P4	O	0	—	—	7.39 ± 0.34	12.22 ± 1.39	13.83 ± 0.33

Data are expressed as the mean ± SEM for at least 3 independent experiments.

Parallel cytotoxicity profiling was undertaken using the non-tumorigenic human mammary epithelial line MCF-10A. The results, presented in **Table 3**, revealed that FK866, Olaparib, and DDY02 each failed to discriminate between breast cancer-derived lines and their normal epithelial counterparts. That said, cell-cycle analysis by flow cytometry showed that DDY02 induced a dose-dependent accumulation of MDA-MB-468 cells in the G1 phase. The imposition of a G1-phase arrest can be strategically exploited to achieve tumor-cell selectivity, driven by the more rapid cycling kinetics of malignant populations compared with normal cells. Altogether, these data suggest that a deeper investigation of the selectivity determinants for dual-target inhibitors of this class is warranted.

Table 3. In vitro anti-proliferative activity of target compounds against MCF-10A cell lines.

Compound	Cytotoxicity IC_{50} *	Cell survival rate (3.0 μM, %) *
FK866	4.41 ± 0.22	65.49 ± 0.41
Olaparib	9.61 ± 0.77	91.76 ± 1.78
Olaparib + FK866	—	65.31 ± 0.03
DDY01	—	67.1 ± 1.73
DDY02	5.31 ± 0.12	70.28 ± 1.06
DDY03	—	80.71 ± 1.5
DDY04	—	98.38 ± 1.74
DDY05	—	88.65 ± 2.41
DDY06	—	69.46 ± 2.56
DDY07	—	70.73 ± 0.07
DDY08	—	72.63 ± 3.46
DDY09	—	66.93 ± 2.45
DDY10	—	96.87 ± 1.71
DDY11	—	82.15 ± 0.21

Data are expressed as the mean ± SEM for at least 3 independent experiments.

DDY02 suppressed colony formation

A clonogenic survival assay was used to evaluate the effects of DDY02, FK866, Olaparib, and the FK866–Olaparib combination on the long-term proliferative capacity of MDA-MB-468 cells. As illustrated in **Figures 6a and 6b**, the inhibition trends derived from colony counting aligned well with those captured by the MTT assay. DDY02 reduced colony output in a concentration-proportional manner. At the 1 μM test level, DDY02 outperformed Olaparib in extinguishing colony formation, though it remained slightly inferior to FK866. The combined FK866 and Olaparib treatment, notably, led to profound suppression of colony growth, further supporting the premise of a synergistic assault on MDA-MB-468 clonogenicity.

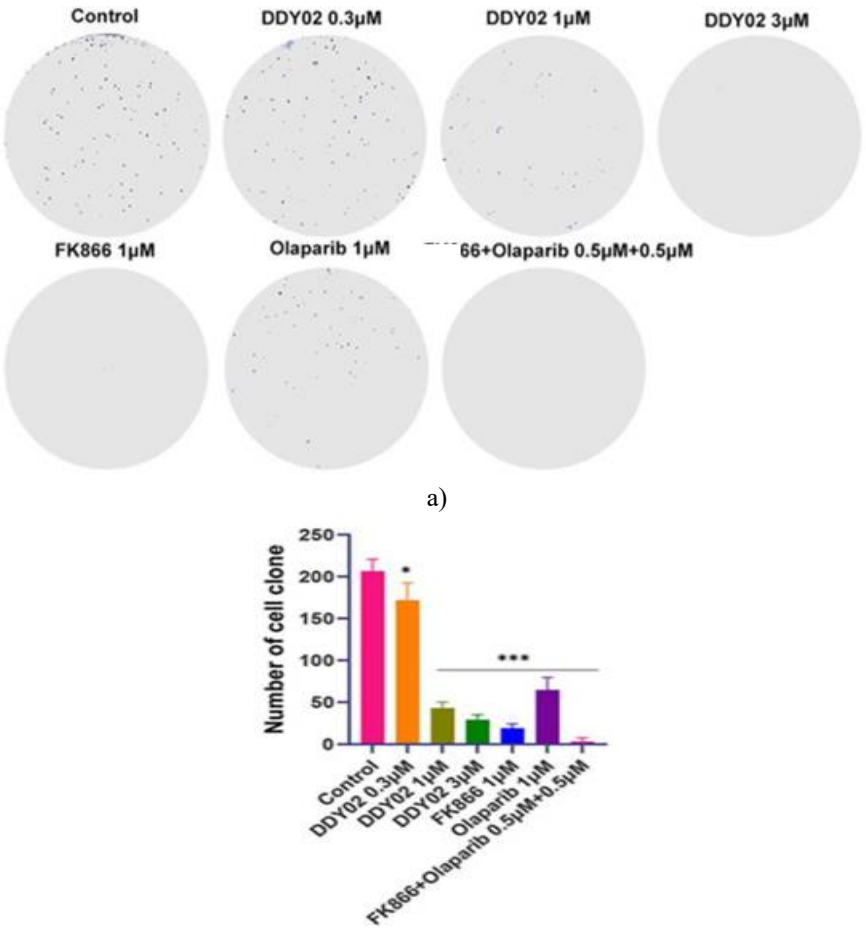

Figure 6. DDY02 inhibited colony formation in MDA-MB-468 cells: (a) Colony formation assay of MDA-MB-468 cells treated with FK866, Olaparib, FK866 + Olaparib, and DDY02, and (b) The number of cell clones in each population. Data are expressed as the mean ± SD (n = 3). $P < 0.05$ and $P < 0.001$ vs. the control group.

NMN reversed the efficacy of compound DDY02

As the direct enzymatic product of the NAMPT-catalyzed step, NMN, when supplied in excess, can functionally bypass the metabolic blockade imposed by NAMPT inhibition. Consistent with this principle, **Figure 7** shows that adding 200 μM NMN to the culture medium substantially blunted the cytotoxicity of both DDY02 and FK866 toward MDA-MB-468 cells. The rescue of cell viability by NMN reinforces the on-target character of DDY02 and validates that its therapeutic impact is intimately coupled to the suppression of NAMPT activity. These observations further raise the possibility of deploying NMN as an interventional tool in therapeutic frameworks centered on NAMPT inhibition.

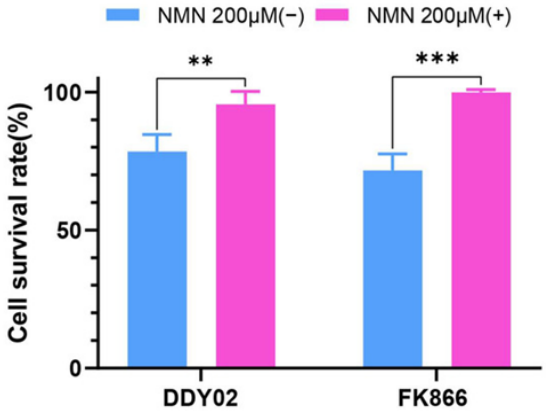

Figure 7. NMN reversed the efficacy of compound DDY02. Data are expressed as the mean ± SD (n = 3). $P < 0.01$ and $P < 0.001$ vs. the control group.

DDY02 reduced cellular NAD levels

Alterations in the intracellular NAD pool following exposure to DDY02, FK866, Olaparib, and the FK866–Olaparib combination were quantified in MDA-MB-468 cells. As summarized in **Figure 8**, a 24 h incubation with DDY02 led to a concentration-dependent fall in NAD content. At 1 μM, DDY02 was nearly as effective as

FK866 at lowering NAD. In contrast, Olaparib, as a single agent at the same concentration, left NAD levels indistinguishable from those of untreated controls. Intriguingly, cells treated with the dual combination (0.5 μM FK866 + 0.5 μM Olaparib) exhibited NAD levels comparable to those observed with 1 μM FK866 alone, demonstrating that co-inhibition enhances NAD depletion.

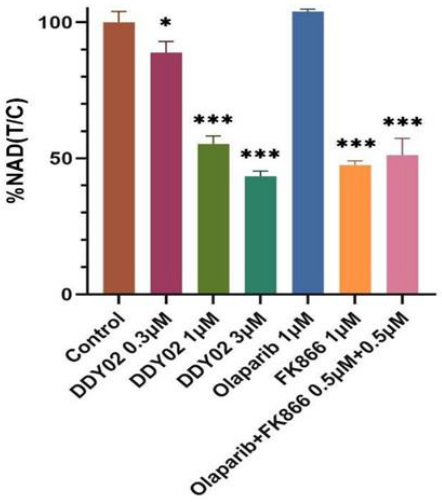

Figure 8. Compound DDY02 reduced the NAD level in MDA-MB-468 cells. Data are expressed as the mean ± SD (n = 3). $P < 0.05$ and $P < 0.001$ vs. the control group.

DDY02 induced DNA damage

The cellular response to single-strand DNA breaks involves rapid PARP1 activation, followed by PARP1-catalyzed poly(ADP-ribosyl)ation of chromatin-associated proteins, which in turn facilitates chromatin decompaction and the recruitment of repair machinery. Pharmacological blockade of PARP1 leaves these single-strand lesions unrepaired; upon fork collision during S phase, they can escalate into double-strand breaks. Phosphorylation of the histone variant H2AX on Ser139—yielding γ-H2AX—provides an accepted early biochemical hallmark of double-strand break formation.

Western blot data presented in **Figure 9a** indicated that DDY02 treatment caused a dose-dependent rise in γ-H2AX abundance in MDA-MB-468 cells. At a uniform 1 μM treatment, DDY02, Olaparib, FK866, and the combination condition each raised γ-H2AX levels, with DDY02 producing the largest increase and Olaparib the smallest. Of particular note, the combination arm led to a more pronounced accumulation of γ-H2AX than either pharmacological agent alone, consistent with the concept that concurrent inhibition of both NAMPT and PARP1 drives enhanced DNA fragmentation.

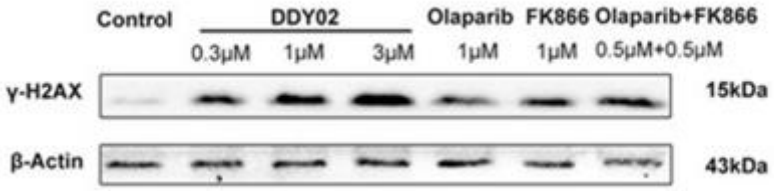

a)

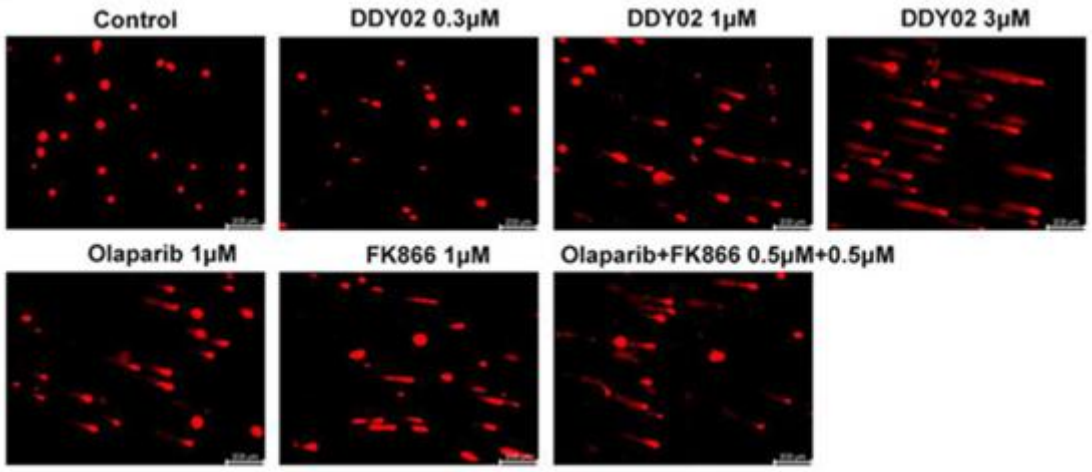

b)

Figure 9. DDY02 induced DNA damage: (a) The effects of FK866, Olaparib, FK866 + Olaparib, and DDY02 on the expression of γ-H2AX were analyzed by Western blot, and (b) Effects of FK866, Olaparib, FK866+ Olaparib, and DDY02 on the DNA damage of MDA-MB-468 cells. The scale bar in the figure represents 200 μm.

Providing orthogonal visual confirmation, the alkaline comet assay **(Figure 9b)** directly imaged DNA lesions in MDA-MB-468 cells **(Figure 9b)**. In full agreement with the immunoblotting results, the extent of DNA damage scaled upward with DDY02 concentration. At the 1 μM dose level, the combination of FK866 and Olaparib produced demonstrably greater tail moments than either compound alone, a result consistent with the notion of synergistic exacerbation of genotoxic stress.

DDY02 induced apoptosis

To probe whether an apoptotic response is mounted by MDA-MB-468 cells upon DDY02 challenge, dual labeling with annexin V and propidium iodide was undertaken, after which flow cytometry resolved the stained populations into four sectors (Q1–Q4) mapping to necrosis (Q1), late apoptosis (Q2), early apoptosis (Q3), and viable cells (Q4).

A dose-dependent escalation in the combined apoptotic fraction (Q2 + Q3) was evident from the data presented in **Figure 10a**: values climbed from 13.34% at 0.3 μM to 21.20% at 1 μM, and reached 48.3% at 3 μM. When comparisons were made at 1 μM, both DDY02 and the FK866–Olaparib pairing induced greater apoptosis than the single-agent treatments. These results position DDY02 as an effective driver of programmed cell death in this TNBC line and demonstrate a synergistic pro-apoptotic effect at the cellular level.

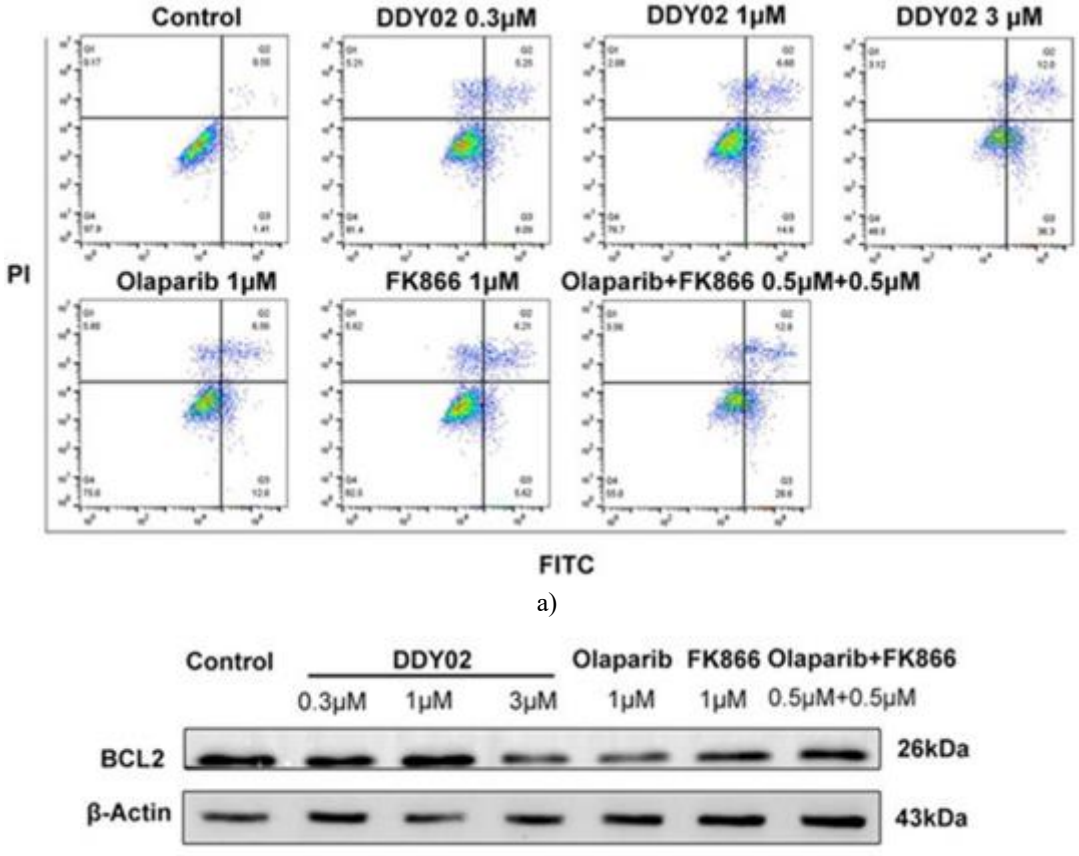

Figure 10. DDY02 induced apoptosis in MDA-MB-468 cells. (a) Cell apoptosis induced by FK866, Olaparib, FK866 + Olaparib, DDY02. (b) The effects of FK866, Olaparib, FK866 + Olaparib, and DDY02 on the expression of BCL2 were analyzed by Western blot.

Subsequent investigation focused on B-cell lymphoma 2 (BCL2), an anti-apoptotic sentinel whose overexpression in TNBC has been causally associated with therapeutic recalcitrance owing to its blockade of drug-induced mitochondrial apoptosis [35, 36]. The rationale for studying BCL2 in this context stems from the recognition that both NAD scarcity—provoked by NAMPT inhibition—and the persistence of DNA lesions—resulting from PARP1 inactivation—can independently route cancer cells toward mitochondrial apoptotic demise [37, 38]. Western blot analysis was therefore performed to determine whether BCL2 levels change under DDY02 treatment. As displayed in **Figure 10b**, a downward trend in BCL2 protein was observed that tracked with increasing DDY02 concentrations. At the 1 μM dose point, Olaparib alone profoundly reduced BCL2, whereas FK866 and the combination regimen produced negligible alterations. One interpretation consistent with these findings is that

DDY02-elicited apoptosis may operate through a PARP1-inhibition-dependent DNA damage axis that subsequently engages the BCL2-regulated mitochondrial death machinery.

DDY02 inhibited cell migration

The preponderance of breast cancer-related mortality can be traced to distant organ colonization by disseminated tumor cells, making the pharmacologic interruption of metastasis a clinical priority for extending patient longevity and quality of life. Overexpression of NAMPT fuels several interrelated cellular programs that jointly facilitate the metastatic aptitude of breast cancer cells. At a fundamental level, the NAMPT-driven expansion of the NAD pool elevates cellular energy charge, potentially endowing malignant cells with the metabolic headroom required for the energy-intensive processes of migration and tissue invasion. Adding another layer, the NAD-dependent deacetylase SIRT1 has been mechanistically linked to the promotion of breast cancer metastasis, and elevated NAD bioavailability may potentiate SIRT1, thereby modulating gene networks that underpin metastatic competence [39]. Moreover, NAMPT upregulation is accompanied by increased production of inflammatory mediators, contributing to a microenvironment that nurtures metastatic outgrowth. The epithelial–mesenchymal transition (EMT) is a developmental reprogramming event in which carcinoma cells lose their polarized epithelial architecture and acquire a spindle-shaped, motile phenotype. PARP1 has been shown to participate in the EMT regulatory circuitry of breast cancer cells, promoting the acquisition of mesenchymal features conducive to metastasis. In keeping with this concept, pharmacological PARP1 blockade using Olaparib has been reported to thwart TGF-β-driven EMT in cancer models [40].

A wound scratch assay served to evaluate the impact of DDY02, FK866, and Olaparib on the motile behavior of MDA-MB-468 cells. In untreated control wells, the denuded area was entirely repopulated within 48 h, as captured in **Figures 11a and 11b**. The strongest blockade of wound closure was observed with Olaparib at 1 μM. DDY02 showed a moderately weaker antimigratory effect, while FK866 ranked as the least inhibitory. Importantly, pushing the DDY02 concentration upward to 3 μM further amplified the degree of migration suppression, establishing a clear concentration–response gradient. These outcomes spotlight DDY02 as a molecule capable of reining in breast cancer cell motility—an attribute of considerable relevance for disrupting the metastatic cascade and altering disease trajectory.

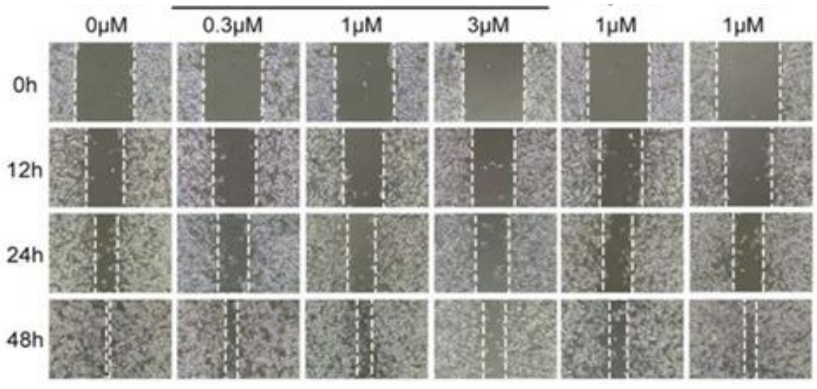

a)

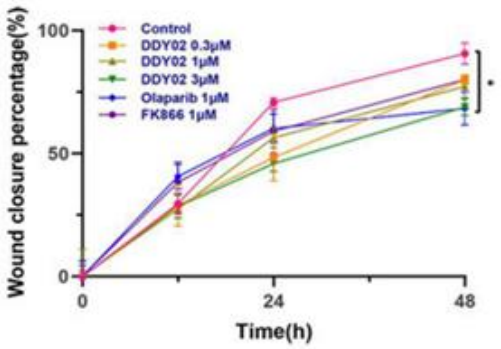

b)

Figure 11. DDY02 inhibits MDA-MB-468 cells' migration in a concentration-dependent manner: (a) Effects of DDY02, FK866, and Olaparib on the migration of MDA-MB-468 cells, and (b) Wound closure percentage of DDY02, FK866, and Olaparib in MDA-MB-468 cells. Data are expressed as the mean ± SD (n = 3). $P < 0.05$ vs. control group.

Conclusion

Among malignancies affecting women across the globe, breast cancer stands out as a particularly grave health threat. Within China, the annual incidence has been on an upward trajectory, and diagnoses are increasingly made in younger populations. Triple-negative breast cancer (TNBC), although it constitutes only 15~20% of breast cancer cases, is the most biologically aggressive form, marked by a heightened likelihood of postsurgical recurrence and metastatic dissemination [41]. Because this subtype lacks expression of ER, PR, and HER-2, it offers no validated molecular targets for tailored therapy. Making matters worse, the period of disease control achieved with standard cytotoxic chemotherapy is shorter in TNBC than in hormone receptor-positive or HER2-amplified disease. For these reasons, the discovery of new anti-TNBC modalities—especially those grounded in unconventional mechanisms of action—has become a pressing objective shared by academic laboratories and the pharmaceutical sector. Reports of dual-target inhibitors that simultaneously engage two tumor-relevant pathways have appeared with increasing frequency and have generated considerable enthusiasm.

Situated at opposing ends of the NAD metabolic pathway are the enzymes NAMPT and PARP1, each performing an essential function. Prior work has documented that pairing NAMPT inhibitors with PARP1 inhibitors produces a cooperative antitumor effect in TNBC models. In the investigation reported here, molecular assembly via pharmacophore fusion yielded a panel of 11 NAMPT/PARP1 dual-target inhibitors. The most distinguished member of this series, DDY02, exerted powerful anti-proliferative activity against MDA-MB-468 cells. The experimental evidence demonstrated that intracellular NAD levels decreased in response to DDY02 in a concentration-dependent manner, and that NMN supplementation partially reversed this growth-inhibitory effect. This finding causally links the pharmacological effect of DDY02 to NAMPT suppression. Evidence from Western blotting and the alkaline comet assay showed that DDY02 also promotes the accumulation of DNA lesions, an effect most plausibly explained by its blockade of PARP1. In addition to these activities, DDY02 was found to drive apoptotic cell death, block cell cycle progression, and reduce the migratory potential of the treated cells.

A candid appraisal of this work must acknowledge several shortcomings that remain to be addressed. The relatively large size of these dual-target molecules, whose molecular weights exceed 600 Da, places them outside the physicochemical parameters outlined by Lipinski's "Rule of Five," raising concerns about oral bioavailability and overall drug-likeness. A further liability is the presence of a pyridine ring, a structural feature that renders compounds susceptible to rapid oxidative processing by cytochrome P450 isozymes, with potentially unfavorable consequences for pharmacokinetic performance. The profound molecular heterogeneity inherent to TNBC also implies that the therapeutic benefit of these inhibitors may not be uniform across all patient subsets, potentially narrowing their clinical reach. It should also be noted that even though the cytotoxic potencies of our synthesized compounds are in the same range as those of the reference drugs, practical obstacles—including limited aqueous solubility, inefficient passage across the plasma membrane, or swift destruction within the intracellular compartment—could erode the synergistic potential that dual-target engagement is intended to confer. Finally, the observation that DDY02 does not sharply distinguish between cancerous and normal breast epithelial cells signals that the safety dimension of this inhibitor class demands deeper scrutiny.

Although intellectual property filings covering NAMPT/PARP1 dual-target inhibitors have been filed, the disclosures within these documents are insufficient to permit a thorough evaluation of their translational promise. The contribution of the present study lies in its role as a foundational proof-of-concept: it supplies a granular view of the design rationale, the structure–activity relationships, and the mechanistic pathways engaged by these compounds. We anticipate that researchers pursuing related lines of inquiry will find value in the data and interpretations presented here. To summarize, our efforts have identified DDY02 as a lead candidate warranting further exploration in TNBC. Work ahead will involve iterative chemical optimization and in vivo animal experimentation to substantiate both its efficacy and toxicological profile.

Acknowledgments: We want to express our gratitude to Li Yunfei of Tianjin University of Traditional Chinese Medicine for his invaluable technical guidance and assistance in conducting biological testing.

Conflict of interest: None

Financial support: This research was funded by the Science & Technology Development Fund of Tianjin Education Commission for Higher Education, grant number 2021KJ126.

Ethics statement: None

References

1. Yaku K, Okabe K, Hikosaka K, Nakagawa T. NAD metabolism in cancer therapeutics. Front Oncol. 2018;8(1):9.

2. Navas LE, Carnero A. Nicotinamide adenine dinucleotide (NAD) metabolism as a relevant target in cancer. Cells. 2022;11(16):2627.
3. Navas LE, Carnero A. NAD metabolism, stemness, the immune response, and cancer. Signal Transduct Target Ther. 2021;6(1):2.
4. Chiarugi A, Dölle C, Felici R, Ziegler M. The NAD metabolome—A key determinant of cancer cell biology. Nat Rev Cancer. 2012;12(11):741–52.
5. Heske CM. Beyond energy metabolism: Exploiting the additional roles of NAMPT for cancer therapy. Front Oncol. 2020;9(1):1514.
6. Tang H, Wang L, Wang T, Yang J, Zheng S, Tong J, et al. Recent advances of targeting nicotinamide phosphoribosyltransferase (NAMPT) for cancer drug discovery. Eur J Med Chem. 2023;258:115607.
7. Wei Y, Xiang H, Zhang W. Review of various NAMPT inhibitors for the treatment of cancer. Front Pharmacol. 2022;13:970553.
8. Galli U, Travelli C, Massarotti A, Fakhfouri G, Rahimian R, Tron GC, et al. Medicinal chemistry of nicotinamide phosphoribosyltransferase (NAMPT) inhibitors. J Med Chem. 2013;56(16):6279–96.
9. Korotchkina L, Kazyulkin D, Komarov PG, Polinsky A, Andrianova EL, Joshi S, et al. OT-82, a novel anticancer drug candidate that targets the strong dependence of hematological malignancies on NAD biosynthesis. Leukemia. 2020;34(7):1828–39.
10. Li X, Li X, Liu F, Li S, Shi D. Rational multitargeted drug design strategy from the perspective of a medicinal chemist. J Med Chem. 2021;64(22):10581–605.
11. Wu Y, Wang L, Huang YH, Chen SQ, Wu SC, Dong GQ, et al. Nicotinamide phosphoribosyltransferase (NAMPT) is a new target of antitumor agent chidamide. ACS Med Chem Lett. 2020;11(1):40–4.
12. Curtin NJ, Szabo C. Poly(ADP-ribose) polymerase inhibition: Past, present and future. Nat Rev Drug Discov. 2020;19(7):711–36.
13. Wang YQ, Wang PY, Wang YT, Yang GF, Zhang A, Miao ZH. An update on poly(ADP-ribose) polymerase-1 (PARP-1) inhibitors: Opportunities and challenges in cancer therapy. J Med Chem. 2016;59(19):9575–98.
14. Zhao Y, Zhang LX, Jiang T, Long J, Ma ZY, Lu AP, et al. The ups and downs of poly(ADP-ribose) polymerase-1 inhibitors in cancer therapy—current progress and future direction. Eur J Med Chem. 2020;203:112570.
15. Zhang J, Zhang J, Li H, Chen L, Yao D. Dual-target inhibitors of PARP1 in cancer therapy: A drug discovery perspective. Drug Discov Today. 2023;28(6):103607.
16. Martínez-Morcillo FJ, Cantón-Sandoval J, Martínez-Navarro FJ, et al. NAMPT-derived NAD+ fuels PARP1 to promote skin inflammation through parthanatos cell death. PLoS Biol. 2021;19(5):e3001455.
17. Bajrami I, Kigozi A, Van WL, Brough R, Frankum J, Lord CJ, et al. Synthetic lethality of PARP and NAMPT inhibition in triple-negative breast cancer cells. EMBO Mol Med. 2012;4(11):1087–96.
18. Heske CM, Davis MI, Baumgart JT, Wilson K, Gormally MV, Chen L, et al. Matrix screen identifies synergistic combination of PARP inhibitors and NAMPT inhibitors in Ewing sarcoma. Clin Cancer Res. 2017;23(24):7301–11.
19. Sauriol A, Carmona E, Udaskin ML, Radulovich N, Leclerc-Desaulniers K, Rottapel R, et al. Inhibition of nicotinamide dinucleotide salvage pathway counters acquired and intrinsic PARP inhibitor resistance in high-grade serous ovarian cancer. Sci Rep. 2023;13(1):3334.
20. Tan C, Zhang X, Yang C, Miao Z, Song S, Huan X, et al. Phthalazone derivative and preparation method and application thereof. CN110194762. 2021.
21. Jiang S, Zhang K, Liao J, Wang D, Ni Y, Wang T, et al. Preparation of phthalozinone compounds and its medical application. CN113788827. 2023.
22. Menear KA, Adcock C, Alonso FC, Blackburn K, Copsey L, Drzewiecki J, et al. Novel alkoxybenzamide inhibitors of poly(ADP-ribose) polymerase. Bioorg Med Chem Lett. 2008;18(12):3942–5.
23. Menear KA, Adcock C, Boulter R, Cockcroft XL, Copsey L, Cranston A, et al. A novel bioavailable inhibitor of poly(ADP-ribose) polymerase-1. J Med Chem. 2008;51(21):6581–91.
24. Giannini G, Battistuzzi G, Vesci L, Milazzo FM, De Paolis F, Barbarino M, et al. Novel PARP-1 inhibitors based on a quinazolinone scaffold. Bioorg Med Chem Lett. 2014;24(3):462–6.
25. Zhou J, Ji M, Zhu Z, Cao R, Chen X, Xu B. Discovery of benzimidazole derivatives as PARP-1 inhibitors with in vivo anti-tumor activity. Eur J Med Chem. 2017;132:26–41.
26. Zheng X, Bauer P, Baumeister T, Buckmelter AJ, Caligiuri M, Clodfelter KH, et al. Structure-based identification of ureas as novel nicotinamide phosphoribosyltransferase (Nampt) inhibitors. J Med Chem. 2013;56(12):4921–37.
27. Xu TY, Zhang SL, Dong GQ, Liu XZ, Wang X, Lv XQ, et al. Discovery and characterization of novel small-molecule inhibitors targeting nicotinamide phosphoribosyltransferase. Sci Rep. 2015;5(1):10043.

28. Dong G, Chen W, Wang X, Yang X, Xu T, Wang P, et al. Small molecule inhibitors simultaneously targeting cancer metabolism and epigenetics: Discovery of novel NAMPT and HDAC dual inhibitors. J Med Chem. 2017;60(20):7965–83.
29. Chen W, Dong G, Wu Y, Zhang W, Miao C, Sheng C. Dual NAMPT/HDAC inhibitors as a new strategy for multitargeting antitumor drug discovery. ACS Med Chem Lett. 2018;9(1):34–8.
30. Dong G, Wu Y, Cheng J, Chen L, Liu R, Ding Y, et al. Ispinesib as an effective warhead for the design of autophagosome-tethering chimeras: Discovery of potent degraders of NAMPT. J Med Chem. 2022;65(21):7619–28.
31. Wu Y, Pu C, Fu Y, Dong G, Huang M, Sheng C. NAMPT-targeting PROTAC promotes antitumor immunity via suppressing MDSC expansion. Acta Pharm Sin B. 2022;12(11):2859–68.
32. Bi K, Cheng J, He S, Fang Y, Huang M, Sheng C, et al. Discovery of highly potent NAMPT degraders for efficient treatment of ovarian cancer. J Med Chem. 2023;66(3):1048–62.
33. Sun D, Dong G, Wu Y, Dong G, Du L, Li M, et al. Fluorescent and theranostic probes for imaging NAMPT. Eur J Med Chem. 2023;248:115080.
34. Lu G, Nie W, Xin M, Meng Y, Gu J, Miao H, et al. Design and synthesis of urea-based benzamide derivatives as PARP-1 inhibitors. Eur J Med Chem. 2022;243:114790.
35. Bouchalova K, Svoboda M, Kharaishvili G, Vrbkova J, Cwiertka K, Manasova D, et al. BCL2 is an independent predictor of outcome in basal-like triple-negative breast cancers. Tumour Biol. 2015;36(6):4243–52.
36. Lindner AU, Lucantoni F, Varešlija D, Holubova M, Rosén A, Kilkelly A, et al. Low cleaved caspase-7 levels indicate unfavourable outcome across all breast cancers. J Mol Med. 2018;96(10):1025–37.
37. Milosevic J, Hoffarth S, Huber C, Schuler M. DNA damage-induced decrease of Bcl-2 is secondary to caspase activation. Oncogene. 2003;22(42):6852–6.
38. Daniels VW, Zoeller JJ, van Gastel N, McCabe NP, Metz RP, Rizzino A, et al. Metabolic perturbations sensitize triple-negative breast cancers to apoptosis induced by BH3 mimetics. Sci Signal. 2021;14(666):eabc7405.
39. Rifaï K, Idrissou M, Penault-Llorca F, Bignon YJ, Bernard-Gallon D. Contradictory roles of SIRT1 in human breast cancer. Cancers (Basel). 2018;10(11):409.
40. Schäcke M, Kumar J, Colwell N, Hermanns HM, Meroni SB, Bartsch JW, et al. PARP-1/2 inhibitor olaparib prevents or reverses EMT induced by TGF-β. Int J Mol Sci. 2019;20(3):518.
41. Garrido-Castro AC, Lin NU, Polyak K. Molecular classifications of triple-negative breast cancer. Cancer Discov. 2019;9(2):176–98.